PAPER

Numerical computations of geometric ergodicity for stochastic dynamics

IOP Publishing | London Mathematical Society Nonlinearity

Nonlinearity **33** (2020) 6935–6970 https://doi.org/10.1088/1361-6544/aba93f

Numerical computations of geometric ergodicity for stochastic dynamics

Yao Li[1,*] **and Shirou Wang**[2]

[1] Department of Mathematics and Statistics, University of Massachusetts Amherst, Amherst, MA, 01002, United States of America
[2] Department of Mathematical and Statistical Sciences, University of Alberta, Edmonton, Alberta, T6G2G1, Canada

E-mail: yaoli@math.umass.edu and shirou@ualberta.ca

Received 9 January 2020, revised 17 July 2020
Accepted for publication 24 July 2020
Published 21 October 2020

Abstract

A probabilistic approach to compute the geometric convergence rate of a stochastic process is introduced in this paper. The goal is to quantitatively compute both the upper and lower bounds for rate of the exponential convergence to the stationary distribution of a stochastic dynamical system. By applying the coupling method, we derive an algorithm which does not rely on the discretization of the infinitesimal generator. In this way, our approach works well for many high-dimensional examples. We apply this algorithm to the random perturbations of both iterative maps and differential equations. We show that the rate of geometric ergodicity of a random perturbed system can, to some extent, reveal the degree of chaoticity of the underlying deterministic dynamics. Various SDE models including the ones with degenerate noise or living on the high-dimensional state space are also explored.

Keywords: stochastic process, stochastic differential equations, geometric ergodicity, coupling method

Mathematics Subject Classification numbers: 37H10, 60J22, 65C99.

(Some figures may appear in colour only in the online journal)

1. Introduction

In this paper, we consider the stochastic processes arising from the random perturbations of deterministic dynamical systems. The dynamics of such a stochastic process, say $\boldsymbol{X} = \{X_t\}$, is a combination of a random diffusion and a deterministic dynamics. The rate of the ergodicity of $\boldsymbol{X}$, i.e., the speed of convergence of the law of X_t to the invariant distribution, is a significant quantity closely related to the spectral gap of the infinitesimal generator of $\boldsymbol{X}$, especially when

*Author to whom any correspondence should be addressed.

$\boldsymbol{X}$ is reversible. From an applied viewpoint, knowing the speed of convergence is very useful to the sampling, uncertainty quantification, and sensitivity analysis [15, 29, 45].

However, the ergodicity of a stochastic process is difficult to study in a quantitative way. Methods based on functional inequalities only work for a limited class of problems such as the over-damped Langevin dynamics [4, 24, 37]. The probabilistic approach, on the other hand, although being 'softer' and more applicable, usually does not give a precise bound in most of the existing results. For instance, by constructing a Lyapunov function and establishing the minorization condition for a certain 'small set', one can easily deduce the geometric ergodicity [22, 23, 44]. Nevertheless, the rate of geometric ergodicity obtained in this way is far from being optimal. In most cases, we only know that the exponential convergence rate to the steady state is $\log \rho$ for some $\rho < 1$, but ρ is usually too close to 1 to be useful in practice.

The computational study of the ergodicity, on the other hand, is far from being mature. While one can compute the eigenvalues of the discretized infinitesimal generator for low-dimensional problems (1D or 2D) as discussed in [27, 36, 48, 49], it does not work well if $\boldsymbol{X}$ lives in a higher dimensional state space. One can obtain the convergence rate through the computation of the correlation decay of a test function by the Monte Carlo simulation. However, as discussed in [38], the correlation (or auto-correlation) has small expectation and large variance, which results in an unrealistic requirement of large amount of samples in the real simulations. In addition, the selection of test functions is very subjective.

The main goal of this paper is to propose a coupling approach, a powerful tool that has been used in many rigorous and computational studies [7, 19, 28, 42, 43], to numerically compute the geometric ergodicity. Traditionally, the coupling method is mainly used in the theoretical study of stochastic dynamics. This is partially because in computations, a numerically simulated trajectory only approximate the real trajectory at discrete times with certain accuracy. As a result, on a continuous state space, two numerical trajectories can easily 'miss' each other even if the actual trajectories have already been coupled together. We solve this by using the maximal coupling whenever two trajectories are sufficiently close and develop a corresponding numerical scheme. By applying to various examples, we show that our numerical coupling algorithm works well for the random perturbed iterative maps, the stochastic differential equations (SDEs) with non-degenerate diffusions, as well as the high-dimensional oscillators. Also, it can be well-adapted to certain systems with degenerate diffusions with some extra computational cost.

A secondary goal of our study is to reveal how the geometric ergodicity of the perturbed stochastic system is related to the complexity of its underlying deterministic dynamics. Applying to the random perturbed circle maps with distinct chaotic properties, we show that the rate of geometric ergodicity, or heuristically the spectral property, can reveal, in some sense, the mixing property of the unperturbed circle maps. For example, as the noise magnitude decreases, the rate of geometric ergodicity drops 'quickly' when the unperturbed dynamics is ergodic but not mixing; while it drops 'dramatically' when the underlying dynamics admits a stable periodic orbit; see section 4 for more details. Our simulation also shows that for the slow-fast systems, a larger time scale separation between the slow and fast dynamics can enhance the geometric convergence rate when the random noises are added. This can be explained by some heuristic arguments with numerical evidence.

The paper is organized as follows. Section 2 provides the necessary probability and dynamical system backgrounds. Results serving as the theoretical basis of this paper are also presented and proved. In section 3, various coupling mechanisms and our numerical algorithms are described. In section 4, by representative examples on the circle, we study the connection between the geometric ergodicity and the chaotic properties of the deterministic dynamics. In

section 5, examples of SDEs with various deterministic or random structures are numerically studied. We conclude this paper in section 6 with some further discussions and potential works.

2. Preliminary

2.1. Markov process and geometric ergodicity

Throughout this paper, let E be a state space, which can be $\mathbb{R}^k$, $\mathbb{T}^k$, or a subset of $\mathbb{R}^k$, endowed with σ-field $\mathcal{B}$. Consider a Markov process $\boldsymbol{X} = \{X_t; t \in \mathcal{T}\}$ on $(E, \mathcal{B})$, where $\mathcal{T}$ can be $\mathbb{R}_{\geqslant 0}, \mathbb{Z}_{\geqslant 0}$, or $h\mathbb{Z}_{\geqslant 0} \coloneqq \{0, h, 2h, \ldots\}$ for $h > 0$. Let $\{P^t(x, A); x \in E, A \in \mathcal{B}, t \in \mathcal{T}\}$ be the transition probabilities of $\boldsymbol{X}$, i.e., for any $t \in \mathcal{T}$, $P^t(\cdot, A)$ is a measurable function for each fixed $A \in \mathcal{B}$, and $P^t(x, \cdot)$ is a probability measure for each fixed $x \in E$ such that

$$P^t(x, \cdot) = \int_E P^s(x, \mathrm{d}y) P^{t-s}(y, \cdot), \quad 0 \leqslant s \leqslant t.$$

In the following, for simplicity we denote the Markov process as $\boldsymbol{X} = \{X_t\}$, the transition probabilities as $\{P^t\}$ when no ambiguity arises.

Given a Markov process $\boldsymbol{X}$ with initial distribution μ, for any $t \in \mathcal{T}$, μP^t is the distribution of $\boldsymbol{X}$ at time t such that

$$\mu P^t(A) = \int_E P^t(x, A) \mu(\mathrm{d}x), \quad \forall\, A \in \mathcal{B}.$$

In particularly, μ is called *invariant* if $\mu P^t = \mu, \forall\, t \in \mathcal{T}$. A Markov process $\boldsymbol{X}$ is said to be *ergodic* if it admits a unique invariant (probability) distribution π such that for any $x \in E$, $A \in \mathcal{B}$,

$$|P^t(x, A) - \pi(A)| \to 0, \quad t \to \infty$$

For a reference measure ϕ on $(E, \mathcal{B})$, $\boldsymbol{X}$ is said to be *ϕ-irreducible* if given any $x \in E$, $\phi(A) > 0$ implies that $P^t(x, A) > 0$ for some $t > 0$. Throughout this paper, we assume that the Markov process $\boldsymbol{X}$ is ergodic with an invariant (probability) distribution π. It is not hard to see that X is π-irreducible.

The emphasis of this paper is the geometric ergodicity. An ergodic Markov process $\boldsymbol{X}$ is said to be *geometrically ergodic* with rate $r > 0$ if for π-a.e. $x \in E$,

$$\limsup_{t \to \infty} \frac{1}{t} \log(\|P^t(x, \cdot) - \pi\|_{\mathrm{TV}}) = -r,$$

where $\|\mu - \nu\|_{\mathrm{TV}} \coloneqq 2 \sup_{A \in \mathcal{B}} |\mu(A) - \nu(A)|$ is the total variation distance between probability measures on $(E, \mathcal{B})$. A Markov process $\boldsymbol{X}$ is said to be *geometrically contracting* with rate $r > 0$ if for $\pi \times \pi$-almost every initial pairs $(x, y) \in E \times E$, it holds that

$$\limsup_{t \to \infty} \frac{1}{t} \log(\|P^t(x, \cdot) - P^t(y, \cdot)\|_{\mathrm{TV}}) = -r.$$

It is easy to see that the geometric ergodicity implies the geometric contraction. Since we already assume the existence of an invariant probability measure, the uniqueness of it directly follows from the geometrically contracting property. On the other hand, in the case of geometric contraction, one usually has estimate

$$\|P^t(x, \cdot) - P^t(y, \cdot)\|_{\mathrm{TV}} \leqslant R(x, y) \mathrm{e}^{-rt}$$

for a prefactor $R(x, y)$. It may happen that the prefactor $R(x, \cdot)$ is too large to be integrable with respect to π, i.e.,

$$\int_E R(x, y)\pi(\mathrm{d}y) = \infty,$$

so that the geometric convergence to the invariant measure π may not be achieve at the same rate $r > 0$.

2.2. Coupling of Markov processes

In this paper, we investigate the geometric ergodicity of Markov processes through the coupling approach. This section serves as the theoretical background of it. We first recall the coupling of measures. Let μ and ν be two probability measures on $(E, \mathcal{B})$. A *coupling* of μ and ν is a probability measure on $E \times E$ whose the first and second marginals are respective μ and ν. There is a well-known inequality showing that the total variation distance between μ and ν is bounded by the difference of random variables realizing them. To be specific, let X and Y be random variables with respective distributions μ and ν. Then (see, for instance, lemma 3.6. in [1])

$$\|\mu - \nu\|_{\mathrm{TV}} \leqslant 2\mathbb{P}[X \neq Y]. \tag{2.1}$$

Let $\boldsymbol{X} = \{X_t; t \in \mathcal{T}\}$ and $\boldsymbol{Y} = \{Y_t; t \in \mathcal{T}\}$ be two stochastic processes on $(E, \mathcal{B})$. A *coupling* of $\boldsymbol{X}$ and $\boldsymbol{Y}$ is a stochastic process $(\boldsymbol{X}, \boldsymbol{Y}) = \{(\mathcal{X}_t, \mathcal{Y}_t); t \in \mathcal{T}\}$ on $E \times E$ such that

(a) The first and second marginal processes $\{\mathcal{X}_t\}$ and $\{\mathcal{Y}_t\}$ are respective copies of $\boldsymbol{X}$ and $\boldsymbol{Y}$;
(b) If $s \in \mathcal{T}$ be such that $\mathcal{X}_s = \mathcal{Y}_s$, then $\mathcal{X}_t = \mathcal{Y}_t$ for all $t \geqslant s$.

The first meeting time of $\mathcal{X}_t$ and $\mathcal{Y}_t$, denoted as $\tau_c := \inf_{t \geqslant 0}\{\mathcal{X}_t = \mathcal{Y}_t\}$, is called the *coupling time*. A coupling $(\boldsymbol{X}, \boldsymbol{Y})$ is said to be *successful* if the coupling time is almost surely finite, i.e., $\mathbb{P}[\tau_c < \infty] = 1$. Throughout this paper, we consider the couplings of two ergodic Markov processes, $\boldsymbol{X}$ and $\boldsymbol{Y}$, with a common transition probabilities $\{P^t\}$ and a (unique) invariant (probability) distribution π. A coupling $(\boldsymbol{X}, \boldsymbol{Y})$ is said to be a *Markov coupling* if $(\boldsymbol{X}, \boldsymbol{Y})$ is a Markov process. A Markov coupling $(\boldsymbol{X}, \boldsymbol{Y})$ is further called *irreducible* if it is $(\pi \times \pi)$-irreducible.

Lemma 2.1. *Let $\boldsymbol{X}$ and $\boldsymbol{Y}$ be Markov processes with a common transition probabilities $\{P^t\}$ and respective initial distributions μ and ν. Then for any coupling $(\boldsymbol{X}, \boldsymbol{Y})$, we have*

$$\|\mu P^t - \nu P^t\|_{TV} \leqslant 2\mathbb{P}[\tau_c > t]. \tag{2.2}$$

Proof. By the definition of coupling time, $\mathcal{X}_t \neq \mathcal{Y}_t$ implies that $\tau_c > t$. Note that μP^t (resp. νP^t) is the distribution of $\mathcal{X}_t$ (resp. $\mathcal{Y}_t$), then (2.2) follows from (2.1). □

The inequality (2.2) is the well-known *coupling inequality*. A coupling $(\boldsymbol{X}, \boldsymbol{Y})$ is said to be *optimal* if the equality in (2.2) is achieved for any $t > 0$. In the present paper, we numerically estimate the rate of geometric ergodicity of $\boldsymbol{X}$ (or $\boldsymbol{Y}$) via (2.2). In practice, it is unrealistic to compute the coupling times for all initial values. Instead, we will develop some theoretical arguments that enable us to extend the result from one initial value to almost all initial values.

Lemma 2.2. *Let $(\boldsymbol{X}, \boldsymbol{Y}) = \{(\mathcal{X}_t, \mathcal{Y}_t)\}$ be an irreducible Markov coupling of Markov processes $\boldsymbol{X}$ and $\boldsymbol{Y}$. Assume that there exists a pair of initial value $(x_0, y_0) \in E \times E$ and a constant $r_0 > 0$ such that*

$$\mathbb{E}_{(x_0,y_0)}[\mathrm{e}^{r_0\tau_c}] < \infty. \tag{2.3}$$

Then (2.3) holds for $(\pi \times \pi)$-almost all initial values.

Proof. Suppose the lemma does not hold. Then there exists a measurable set $A \subseteq E \times E\backslash\{(x,x) : x \in E\}$ with $(\pi \times \pi)(A) > 0$ such that for any pair $(x,y) \in A$,

$$\mathbb{E}_{(x,y)}[\mathrm{e}^{r_0\tau_c}] = \infty. \tag{2.4}$$

By the irreducibility, there exists $T > 0$ such that $\mathbb{P}_{(x_0,y_0)}[(\mathcal{X}_T, \mathcal{Y}_T) \in A] > 0$. Then by (2.4), together with the Markov property, we have

$$\begin{aligned}\mathbb{E}_{(x_0,y_0)}[\mathrm{e}^{r_0\tau_c}] &\geqslant \int_{(\mathcal{X}_T,\mathcal{Y}_T)\in A} \mathrm{e}^{r_0\tau_c}\mathrm{d}\mathbb{P}_{(x_0,y_0)} \\ &\geqslant \mathbb{P}_{(x_0,y_0)}[(\mathcal{X}_T, \mathcal{Y}_T) \in A] \cdot \int_{(\mathcal{X}_T,\mathcal{Y}_T)\in A} \mathrm{e}^{r_0\tau_c}\mathrm{d}\mathbb{P}_T \\ &= \mathbb{P}_{(x_0,y_0)}[(\mathcal{X}_T, \mathcal{Y}_T) \in A] \cdot \mathbb{E}_\mu[\mathrm{e}^{r_0(\tau_c - T)}] = \infty,\end{aligned}$$

where $\mathbb{P}_T$ is the conditional probability measure of $\mathbb{P}_{(x_0,y_0)}$ conditioning on $(\mathcal{X}_T, \mathcal{Y}_T) \in A$, and μ is the distribution of $(\mathcal{X}_T, \mathcal{Y}_T)$ conditional on A. This contradicts with (2.3). □

One problem with lemma 2.2 is that many efficient couplings we shall use, such as the synchronous coupling and reflection coupling (see section 3 for the concrete meaning), are not irreducible. On the other hand, although the independent coupling (i.e., the two marginal processes are updated independently all the time) brings about the irreducibility, it is usually not efficient for the coupling process. In fact, most stochastic processes in $\mathbb{R}^k$ (e.g., a strong-Feller process), including all the numerical examples in this paper, are *non-atomic*, which means that any two independent trajectories of $\boldsymbol{X}$, say X_t^1 and X_t^2, satisfy $\mathbb{P}[X_{t+1}^1 = X_{t+1}^2 \,|\, X_t^1 \neq X_t^2] = 0$ (without loss of generality, here we assume that $\mathcal{T} = \mathbb{Z}_{\geqslant 0}$). So the independent coupling of a non-atomic Markov process has zero probability of being coupled successfully in finite time.

To overcome this difficulty, we introduce the coupling with independent components. Still, without loss of generality, we assume $\mathcal{T} = \mathbb{Z}_{\geqslant 0}$. *A coupling with independent components* means that at each step before being coupled, with a positive probability (which tough can be very small), the two marginal processes are updated in an independent way. The following lemma shows that a coupling with independent components of a non-atomic Markov process is irreducible. Thus, we can use a mixture of the independent coupling and other more efficient couplings to achieve both the irreducibility and the coupling efficiency.

Lemma 2.3. *Let $(\boldsymbol{X}, \boldsymbol{Y}) = \{(\mathcal{X}_t, \mathcal{Y}_t)\}$ be a coupling with independent components of non-atomic Markov processes $\boldsymbol{X}$ and $\boldsymbol{Y}$. Then $(\boldsymbol{X}, \boldsymbol{Y})$ is $(\pi \times \pi)$-irreducible.*

Proof. It is sufficient to show that for any product set $A_1 \times A_2 \in \mathcal{B} \times \mathcal{B}$ with positive $\pi \times \pi$ measure, there exists some $t_0 \in \mathcal{T}$ such that $\mathbb{P}[(\mathcal{X}_{t_0}, \mathcal{Y}_{t_0}) \in A_1 \times A_2] > 0$.

By the ergodicity, since $A_1 \in \mathcal{B}$ has positive π-measure, there exists $T_1 > 0$ such that $\mathbb{P}[\mathcal{X}_t \in A_1] > 0$ for all $t > T_1$. Similarly, there exists $T_2 > 0$ such that $\mathbb{P}[\mathcal{Y}_t \in A_2] > 0$ for all $t > T_2$. Let $t_0 = \max\{T_1, T_2\} + 1$. Because there is a positive probability that independent updates be chosen for $t = 0, 1, \ldots, t_0$, and the Markov process is non-atomic, we have $\mathbb{P}[(\mathcal{X}_{t_0}, \mathcal{Y}_{t_0}) \in A_1 \times A_2] > 0$. □

Lemma 2.4. *Let $(\boldsymbol{X}, \boldsymbol{Y})$ be a coupling with independent components of non-atomic Markov processes $\boldsymbol{X}$ and $\boldsymbol{Y}$. Assume that there exist an initial value $x_0 \in E$ and a constant $r_0 > 0$ such that*

$$\mathbb{E}_{(x_0,\pi)}[\mathrm{e}^{r_0\tau_c}] < \infty. \tag{2.5}$$

Then (2.5) holds for π-a.e. initial values $x \in E$.

Proof. Suppose the lemma does not hold. Then there exists a measurable set $A \subseteq E$ with $\pi(A) > 0$ such that for any $x \in A$,

$$\mathbb{P}_{(x,\pi)}[e^{r_0\tau_c}] = \infty.$$

Now let $\mathcal{X}_0 = x_0$ and $\mathcal{Y}_0 \sim \pi$. By the irreducibility of $\boldsymbol{X}$, there exists a finite time $T > 0$ such that $P^T(x_0, A) > 0$. Denote λ_A and π_A as the conditional measure of $P^T(x_0, \cdot)$ and π on A, respectively. Since $(\boldsymbol{X}, \boldsymbol{Y})$ is a coupling with independent components, the probability that $\mathcal{X}_t$ and $\mathcal{Y}_t$ remain being independent with each other for $t = 0, 1, \ldots, T$ is strictly positive. Since the Markov processes $\boldsymbol{X}$ and $\boldsymbol{Y}$ are non-atomic. Then with probability 1, the independent updates will not make $\boldsymbol{X}$ and $\boldsymbol{Y}$ couple. Hence, there exists a positive number $\delta > 0$ such that

$$\mathbb{P}_{(x_0,\pi)}[(\mathcal{X}_T, \mathcal{Y}_T) \in C] \geqslant \delta \cdot (P^T(x_0, \cdot) \times \pi)(C), \quad \forall\ C \subseteq E \times E.$$

Applying the similar arguments as in lemma 2.2, we have

$$\mathbb{E}_{(x_0,\pi)}[e^{r_0\tau_c}] \geqslant \delta \cdot P^T(x_0, A)\pi(A)\mathbb{E}_{\lambda_A\times\pi_A}[e^{r_0(\tau_c - T)}] = \infty.$$

This contradicts to (2.5). □

It follows from lemmas 2.2–2.4 that for any coupling with independent components, the finiteness of $\mathbb{E}[e^{r_0\tau_c}]$ can be generalized from one pair of initial values to almost all pairs. By the Markov inequality, we have

$$\mathbb{P}[\tau_c \geqslant t] \leqslant \mathbb{E}[e^{r_0\tau_c}]e^{-r_0 t}.$$

Then together with the coupling inequality (2.2), the finiteness of $\mathbb{E}[e^{r_0\tau_c}]$ yields the geometric contraction/ergodicity. However, the moment generating function $\mathbb{E}[e^{r_0\tau_c}]$ is difficult to compute in practice, especially when r_0 is close to the critical value $\sup\{r > 0 : \mathbb{E}[e^{r\tau_c}] < \infty\}$. To overcome this, we turn to the estimate of the exponential tail of $\mathbb{P}[\tau_c > t]$ instead. This is justified by the following lemma.

Lemma 2.5. *For any initial distributions μ and ν, assume that for $r_0 > 0$,*

$$\limsup_{t\to\infty} \frac{1}{t} \log\ \mathbb{P}_{(\mu,\nu)}[\tau_c > t] \leqslant -r_0. \tag{2.6}$$

Then for any $\epsilon \in (0, r_0)$, it holds that

$$\mathbb{E}_{(\mu,\nu)}[e^{(r_0-\epsilon)\tau_c}] < \infty.$$

Proof. By (2.6), for any $\epsilon \in (0, r_0)$, there exists $t_\epsilon < \infty$ such that for all $t \geqslant t_\epsilon$, it holds that

$$\mathbb{P}_{(\mu,\nu)}[\tau_c > t] \leqslant e^{-(r_0-\epsilon/2)t}.$$

Thus, for any $N > t_\epsilon$,

$$\begin{aligned}\mathbb{E}_{(\mu,\nu)}[e^{(r_0-\epsilon)\tau_c} \cdot 1_{\tau_c>N}] &\leqslant \sum_{i=N}^{\infty} e^{(i+1)(r_0-\epsilon)}\mathbb{P}[\tau_c = i] \\ &\leqslant \sum_{i=N}^{\infty} e^{(i+1)(r_0-\epsilon)}e^{-(r_0-\epsilon/2)i} = e^{(r_0-\epsilon)}\sum_{i=N}^{\infty} e^{-i\epsilon/2},\end{aligned}$$

which goes to zero as N goes to infinity. Hence, $\mathbb{E}_{(\mu,\nu)}[e^{(r_0-\epsilon)\tau_c}]$ must be finite. □

Combine the above lemmata together, we have the following.

Proposition 2.6. *Let $(\boldsymbol{X}, \boldsymbol{Y})$ be a coupling with independent components of non-atomic Markov processes $\boldsymbol{X}$ and $\boldsymbol{Y}$.*

(*a*) *Assume that there exist an initial pair $(x_0, y_0) \in E \times E$ and $r_0 > 0$ such that*

$$\limsup_{t\to\infty} \frac{1}{t} \log \mathbb{P}_{(x_0,y_0)}[\tau_c > t] \leqslant -r_0.$$

Then for any $\epsilon \in (0, r_0)$, $\boldsymbol{X}$ (or $\boldsymbol{Y}$) is geometrically contracting with rate $(r_0 - \epsilon)$;

(*b*) *Assume that there exist $x_0 \in E$ and $r_0 > 0$ such that*

$$\limsup_{t\to\infty} \frac{1}{t} \log \mathbb{P}_{(x_0,\pi)}[\tau_c > t] \leqslant -r_0.$$

Then for any $\epsilon \in (0, r_0)$, $\boldsymbol{X}$ (or $\boldsymbol{Y}$) is geometrically ergodic with rate $(r_0 - \epsilon)$.

2.3. An upper bound of the geometric rate

In general, the coupling inequality (2.2) only gives a lower bound of the geometric convergence/contraction rate. We argue that in some cases, e.g., the random perturbation of a logistic map considered in section 4.4, the upper bound of the geometric ergodicity can be also estimated by using the first passage times because of the existence of the optimal coupling.

For sake of simplicity, we consider the discrete-time Markov processes. Recall that a coupling is said to be optimal if the equality in (2.2) holds for all times. It has been shown that for any two mutually singular probabilities μ and ν, an optimal coupling with initial distribution $\mu \times \nu$ exists and was explicitly constructed in [21, 47].

Proposition 2.7. *Let $\boldsymbol{X} = \{X_n; n \in \mathbb{Z}_{\geqslant 0}\}$ and $\boldsymbol{Y} = \{Y_n; n \in \mathbb{Z}_{\geqslant 0}\}$ be Markov processes on E with initial conditions $X_0 = x$ and $Y_0 = y$, respectively, where $x \neq y$. Let $\{(A_n, B_n)\}_{n=0}^{\infty}$ be a sequence of disjoint pairs of subsets in $E \times E$ such that $x \in A_0$, $y \in B_0$. Assume that*

$$\rho := \limsup_{n\to\infty} \frac{1}{n} \log \mathbb{P}[\min\{\eta_x, \eta_y\} > n] > 0,$$

where

$$\eta_x = \min_{n>0}\{X_n \in A_n^c\}, \qquad \eta_y = \min_{n>0}\{Y_n \in B_n^c\}.$$

Then if $\boldsymbol{X}$ (or $\boldsymbol{Y}$) is geometrically contracting with rate $r > 0$, we have $r \leqslant \rho$.

Proof. Let $(\boldsymbol{X}, \boldsymbol{Y}) = \{(\mathcal{X}_n, \mathcal{Y}_n)\}$ be the optimal coupling of $\boldsymbol{X}$ and $\boldsymbol{Y}$. Then we have

$$\|P^n(x, \cdot) - P^n(y, \cdot)\|_{\mathrm{TV}} = 2\mathbb{P}[\tau_c > n],$$

where $\{P^t\}$ is the common transition probabilities of $\boldsymbol{X}$ and $\boldsymbol{Y}$. Note that at the coupling time τ_c, we have $\mathcal{X}_{\tau_c} = \mathcal{Y}_{\tau_c}$. This means that before time τ_c, either $\mathcal{X}_n$ has exited from A_n or $\mathcal{Y}_n$ has exited from B_n, i.e., $\tau_c \leqslant n$ implies $\min\{\tilde{\eta}_x, \tilde{\eta}_y\} \leqslant n$. Here, $\tilde{\eta}_x, \tilde{\eta}_y$ are defined similarly as η_x, η_y, but for the $\mathcal{X}_n, \mathcal{Y}_n$ instead. By noting that for any $n \geqslant 0$, $\mathcal{X}_n$ (resp. $\mathcal{Y}_n$) has the same distribution as X_n (resp. Y_n), we have

$$\mathbb{P}[\min\{\eta_x, \eta_y\} > n] = \mathbb{P}[\min\{\tilde{\eta}_x, \tilde{\eta}_y\} > n] < \mathbb{P}[\tau_c > n].$$

This completes the proof. □

In section 4.4, for a random perturbed circle map with a stable 2-periodic orbit, we shall give both upper and lower bounds of the geometrically ergodic rate through the first exit times and the coupling times, receptively.

2.4. Deterministic dynamics and random perturbations

Throughout this paper, by a discrete- or continuous-time deterministic dynamical system, we mean by iterating a map

$$f : E \to E, \tag{2.7}$$

or an ordinary differential equation

$$\mathrm{d}Z_t/\,\mathrm{d}t = g(Z_t), \quad t \in \mathbb{R} \tag{2.8}$$

where g is a vector field on E which is locally Lipschitz continuous.

In this paper, we mainly focus on the Markov processes arising from the random perturbations of a deterministic dynamical system. To be specific, we shall consider

(a) The random perturbation of a discrete-time dynamics (2.7)

$$X_{n+1} = f(X_n) + \zeta_n, \tag{2.9}$$

where $\{\zeta_n\}$ are independent random variables taking values in E which will be defined specifically in each particular situation;

(b) The random perturbation of a continuous-time dynamics (2.8) given by a SDE on $\mathbb{R}^k$,

$$\mathrm{d}X_t = g(X_t)\,\mathrm{d}t + \sigma(X_t)\,\mathrm{d}W_t, \tag{2.10}$$

where $\sigma(\cdot)$ is a $k \times k$ matrix-valued function and W_t is a Wiener process on $\mathbb{R}^k$. Here, g and σ are assumed to be smooth enough to give a well-defined solution X_t for all $t > 0$.

In the remainder of this section, we briefly review a classical hierarchy of chaotic properties of deterministic dynamical systems, from the ergodicity to mixing. Readers may refer to [31, 52] for more details. For sake of clarity and more fitting to the situation in section 4, we use intuitive examples of maps on $\mathbb{S}^1$, which are definitely not essential restrictions.

Irrational rotations and ergodicity. A deterministic map $f_\alpha : \mathbb{S}^1 \to \mathbb{S}^1$ is said to be an irrational rotation (or quasi-periodic) if $f_\alpha x = x + \alpha \pmod 1$, where α is an irrational number. Irrational rotation on $\mathbb{S}^1$ exhibits certain regular recurrent behaviour that starts from any arbitrary initial point, the trajectory will visit any interval subsets in certain 'periodic' way. This is in fact what the ergodic property says.

For a deterministic dynamics f, the measure-theoretically chaotic property is usually defined with respect to certain f-invariant measure m, i.e., $m(fA) = m(A)$. An f-invariant measure m is said to be ergodic if for any $\varphi \in C^0(E)$, $\psi \in L^1(m)$, it holds that

$$\frac{1}{n}\sum_{i=0}^{n-1} \int \varphi(f^i x)\psi(x)\mathrm{d}m(x) \to \int \varphi \mathrm{d}m \int \psi \mathrm{d}m, \quad n \to \infty. \tag{2.11}$$

Another (and more well-known) characterization of ergodicity is through the Birkhoff ergodic theorem. For any $\varphi \in L^1(m)$, for m-a.e. $x \in E$, it holds that

$$\frac{1}{n}\sum_{i=0}^{n-1} \varphi(f^i x) \to m(A), \quad n \to \infty \tag{2.12}$$

if f is ergodic with respect to m. The expression (2.12) basically says that a typical trajectory visits any positive-measured set repeatedly with frequency of the set measure. The irrational rotation on $\mathbb{S}^1$ is ergodic with respect to the Lebesgue measure which is also the unique invariant measure.

Expanding maps and mixing. The rotations on $\mathbb{S}^1$ only indicate a low-complexity of chaotic properties since different orbits exhibits similar asymptotic behaviours. To characterize more non-trivial chaotic behaviours, certain expanding properties are expected. A smooth circle map f is said to be *expanding* if it always holds that $|f'| \geqslant 1$. An expanding map is further called uniform expanding if $|f'|$ is uniformly away from 1. An expanding map often comes with the mixing property. An f-invariant measure m is said to be *(strong) mixing* if for any $\varphi \in C^0(E)$, $\psi \in L^1(m)$, it holds that

$$\int \varphi(f^n x)\psi(x)\mathrm{d}m(x) \to \int \varphi \mathrm{d}m \int \psi \mathrm{d}m, \quad n \to \infty. \tag{2.13}$$

A mixing measure is said to be *exponentially (resp. polynomially) mixing* if (2.13) converges in the exponential (resp. polynomial) way. It is well-known that the uniform expanding maps are exponential mixing. For a general (non-uniform) expanding map however, the exponential mixing property may be lost. A classical example illustrating this is the expanding map with the only one neutral fixed point; see section 4.2 for more details.

An intuitive way to understand the chaotic properties of ergodicity and mixing is to look at how two different subsets (measure-theoretically) meet with each other under evolutions. Taking $\varphi = \chi_A, \psi = \chi_B$ where A, B are two measurable subsets, respectively. The ergodicity property (2.11) (resp. mixing property (2.13)) yields

$$\frac{1}{n}\sum_{i=0}^{n-1} m(f^{-i}A \cap B) \to m(A)m(B), \quad n \to \infty$$

$$(\text{resp. } m(f^{-n}A \cap B) \to m(A)m(B), \quad n \to \infty.)$$

It is not hard to see that the ergodicity property is mild which can be guaranteed if any two subsets can meet with each other in a 'regular' way (for instance, the irrational rotations on $\mathbb{S}^1$); on the other hand, the mixing property requires a certain kind of 'stretching' of the system so that any two subsets can meet with each other eventually and forever. By this, we see that the mixing is a stronger property than the ergodicity.

In section 4, we shall use four examples of circle maps with the degree of chaoticity goes down from the exponentially/polynomially mixing to the ones without any mixing behaviours (which even exhibit contraction properties). We observe that although the geometric ergodicity usually holds when random noises are added, the rate can vary, as the noise vanishes, in different ways if the unperturbed dynamics exhibits distinct level of complexities. Again, we remark that the $\mathbb{S}^1$ setting is only for convenience. The scenario should be observed in more general state space.

2.5. Numerical scheme of SDEs

In the real simulations, an SDE is numerically computed at discrete times. We usually choose a time step size $0 < h \ll 1$ and consider the discrete-time trajectories $X_0, X_h, \ldots, X_{nh}, \ldots$. To avoid confusion and make notations consistent, let $\boldsymbol{X} = \{X_t; t \in \mathbb{R}_{\geqslant 0}\}$ be the true trajectories of the SDE, and $\bar{\boldsymbol{X}} = \{\bar{X}_t; t \in h\mathbb{Z}_{\geqslant 0}\}$ be the trajectories of the numerical integrator. In addition, we denote $\boldsymbol{X}^h = \{X_n^h; n \in \mathbb{Z}_{\geqslant 0}\}$ as the time-h sample chain of $\boldsymbol{X}$ such that $X_n^h = X_{nh}$, and $\bar{\boldsymbol{X}}^h = \{\bar{X}_n^h; n \in \mathbb{Z}_{\geqslant 0}\}$ as the time-h sample chain of $\bar{\boldsymbol{X}}$ with $\bar{X}_n^h = \bar{X}_{nh}$.

The most commonly used numerical schemes of SDE (2.10) is the Euler–Maruyama scheme

$$\bar{X}_{(n+1)h} = \bar{X}_{nh} + g(\bar{X}_{nh})h + \sigma(\bar{X}_{nh})\sqrt{h}N_n,$$

where $\{N_n\}$ are standard normal random variables independent for each n. Note that the time-h sample chain $\bar{X}_n^h$ fits the setting of discrete-time random perturbed dynamics (2.9)

$$\bar{X}_{n+1}^h = \bar{X}_n^h + g(\bar{X}_n^h)h + \sigma(\bar{X}_n^h)\sqrt{h}N_n.$$

The Euler–Maruyama method can be improved to the Milstein method. The 1D Milstein method reads as

$$X_{(n+1)h} = X_{nh} + f(X_{nh})h + \sigma(X_{nh})\sqrt{h}N_n + \frac{1}{2}\sigma(X_{nh})\sigma'(X_{nh})(N_n^2 - 1)h.$$

In particular, on any dimensions, the Euler–Maruyama method coincides with the Milstein method if $\sigma(X_t)$ is a constant matrix.

Now, we recall the strong and weak approximations defined in [35]. Let $T < \infty$ be a given finite time. If for $\gamma > 0$,

$$\mathbb{E}[|\bar{X}_T - X_T|] \leqslant C(T)h^\gamma$$

holds for all sufficiently small $h > 0$, then we say that $\bar{\boldsymbol{X}}$ converges *strongly* to $\boldsymbol{X}$ with the order γ. Let C_P^ℓ denote the space of ℓ times continuously differentiable functions with polynomial growth rate for both the function itself and all the partial derivatives up to order the ℓ. If for $\gamma > 0$, any test function $g \in C_P^{2(\gamma+1)}$ and any given finite time T, we have

$$|\mathbb{E}[g(\bar{X}_T)] - \mathbb{E}[g(X_T)]| \leqslant C(T)h^\gamma,$$

then we say that $\bar{\boldsymbol{X}}$ converges to $\boldsymbol{X}$ *weakly* with order γ. It is well known that under suitable regularity conditions, the Euler–Maruyama scheme has strong convergence with order 0.5 and weak convergence with order 1.0. The Milstein scheme has strong convergence with order 1.0 [35].

3. Description of algorithm

The main idea of this paper is to use the exponential tail of the coupling time distributions to numerically estimate the geometric ergodicity of a stochastic process. Assume that for a pair of initial values (x_0, y_0) we have

$$\mathbb{P}_{x_0,y_0}[\tau_c > t] \approx C\mathrm{e}^{-rt}, \quad \forall\ t \gg 1.$$

It follows from proposition 2.6 that for almost every pair of initial values (x, y),

$$\limsup_{t\to\infty} \frac{1}{t}\ \log(\|P^t(x,\cdot) - P^t(y,\cdot)\|_{\mathrm{TV}}) < -r.$$

Replacing y by a sampling from the invariant distribution π, the numerical verification of geometric ergodicity is also obtained by this approach.

Since this paper studies the coupling times in a numerical way, we consider, for the sake of definiteness, the time-discrete Markov process $\boldsymbol{X} = \{X_n; n \in \mathbb{Z}_{\geqslant 0}\}$ as it fits both cases of random perturbations of an iterative mapping and the time-h sample chain of an SDE. Note that here, the $n \in \mathbb{Z}_{\geqslant 0}$ corresponds to the number of iterations or numerical steps. For sake

of differentiation and clarity, in the SDE setting, we will use n_c to denote the numerical steps needed for a successful coupling, which of course depends on the step size h. The physical coupling time will be $\tau_c = n_c h$.

3.1. Coupling methods

Consider a Markov coupling $(\boldsymbol{X}, \boldsymbol{Y})$. In the theoretical proof, a coupling is usually done by making trajectories of both $\boldsymbol{X}$ and $\boldsymbol{Y}$ enter a 'small set' which satisfies the minorization condition [44]. Numerically however, these couplings are not the most efficient ones. We will use a mixture of the following coupling methods to achieve the numerical coupling efficiently.

Independent coupling. Independent coupling means that when running the coupling process $(\boldsymbol{X}, \boldsymbol{Y})$, the noise terms in the two marginal processes $\mathcal{X}_n$ and $\mathcal{Y}_n$ are independent until they are coupled. In other words, we have

$$(\mathcal{X}_{n+1}, \mathcal{Y}_{n+1}) = \left(f(\mathcal{X}_n) + \zeta_n^1, f(\mathcal{Y}_n) + \zeta_n^2\right),$$

where for each n, (ζ_n^1, ζ_n^2) is a pair of independent random variables. In the theoretical studies, independent coupling is frequently used combined with the renewal theory to show the different rates of convergence to the invariant probability measure. In this paper, the independent coupling is to make the coupling process admit independent components so that lemmas 2.3 and 2.4 are applicable.

Synchronous coupling. Another commonly approach to coupling two processes is the synchronous coupling. Contrary to the independent coupling for which the randomness in the two stochastic trajectories are totally unrelated, in the synchronous coupling, we always put the same randomness to the both marginal processes until they are coupled, i.e.,

$$(\mathcal{X}_{n+1}, \mathcal{Y}_{n+1}) = \left(f(\mathcal{X}_n) + \zeta_n^1, f(\mathcal{Y}_n) + \zeta_n^2\right),$$

where $\zeta_n^1 = \zeta_n^2$ for any $n < n_c$. The advantage of the synchronous coupling is that if the deterministic part of the system already admits some kind of stability, then $\mathcal{X}_n$ will approach to $\mathcal{Y}_n$ quickly when the same noise is added each time [2]. The synchronous coupling not only requires less assumptions on the random terms, but also builds some potential connections between the random dynamical system and SDEs; see section 5.4 for a concrete example of the implementation of the synchronous coupling.

Reflection coupling. When the dimension of the state space is greater than 2, two Wiener processes will meet less often than the one/two dimensional case. This makes the independent coupling less effective. The reflection coupling will play a role instead. As an example, take the Euler–Maruyama scheme of the SDE

$$\bar{X}_{n+1}^h = \bar{X}_n^h + f(\bar{X}_n^h)h + \sigma\sqrt{h}N_n,$$

where σ is an invertible constant matrix, and N_n is a normal random variable with mean zero and covariance matrix Id_k. The reflection coupling means that we run the time-h chain $\bar{X}_n^h$ as

$$\bar{X}_{n+1}^h = \bar{X}_n^h + f(\bar{X}_n^h)h + \sigma\sqrt{h}N_n;$$

while run $\bar{Y}_n^h$ as

$$\bar{Y}_{n+1}^h = \bar{Y}_n^h + f(\bar{Y}_n^h)h + \sigma\sqrt{h}PN_n,$$

where $P = I - 2e_n e_n^\top$ is a projection matrix with

$$e_n = \frac{\sigma^{-1}(\bar{X}_n^h - \bar{Y}_n^h)}{\|\sigma^{-1}(\bar{X}_n^h - \bar{Y}_n^h)\|}.$$

In other words, the noise term is reflected against the hyperplane that orthogonally passes the midpoint of the line segment connecting $\bar{X}_n^h$ and $\bar{Y}_n^h$.

Theoretically, it has been proved that for the Brownian motions, the reflection coupling is optimal [26, 43], i.e, the equality in (2.2) is achieved for any $t > 0$. It also works well for many SDEs [9, 10, 17, 18, 43], including the Langevin dynamics with degenerate noise [7, 19]. The reflection coupling introduced above is also applicable to some non-constant σ under suitable assumptions [43]. However, for a general non-constant $\sigma(x)$, the 'true reflection' is given by the Kendall–Cranston coupling with respect to the Riemannian matrix $\sigma^T(x)\sigma(x)$ [12, 25, 32], which is more difficult to implement numerically.

Maximal coupling. In the numerical simulations, the above three couplings can only bring $\mathcal{X}_n$ close to $\mathcal{Y}_n$. We still need a mechanism to make $\mathcal{X}_{n+1} = \mathcal{Y}_{n+1}$ with certain probability. The maximal coupling aims to achieve this. It is derived to couple two trajectories as much as possible at the next step, which is in fact modified from the now well-known Doeblin coupling [16]. We adopt the name 'maximal coupling' from [28].

Assume that at certain step n, $(\mathcal{X}_n, \mathcal{Y}_n)$ takes the value $(x, y) \in E \times E$. Denote the probability measures associated with $f(x) + \zeta_n^1$ and $f(y) + \zeta_n^2$ by μ_x and μ_y, respectively. Let $\nu_{x,y}$ be the 'minimum probability measure' of μ_x and μ_y such that

$$\nu_{x,y}(A) = \frac{1}{\eta} \min\{\mu_x(A), \mu_y(A)\},$$

where η is a normalizer to make $\nu_{x,y}$ a probability measure. At the next step, $(\mathcal{X}_{n+1}, \mathcal{Y}_{n+1})$ is sampled such that

- with probability $(1 - \eta)$,

$$\mathcal{X}_{n+1} \sim \frac{1}{1-\eta}(\mu_x - \eta\nu_{x,y}), \qquad \mathcal{Y}_{n+1} \sim \frac{1}{1-\eta}(\mu_y - \eta\nu_{x,y})$$

- with probability η,

$$\zeta_n^1 = \zeta_n^2 \sim \nu_{x,y}.$$

In other words, $\boldsymbol{X}$ and $\boldsymbol{Y}$ are coupled if and only if the two samples fall into a 'common future' simultaneously. We remark that the classical version of Doeblin coupling requires that the two trajectories enter a certain predefined 'small set' simultaneously. Then a construction called the Nummelin split guarantees them to be coupled with certain positive probability. However, such a construction becomes unnecessary when running the numerical simulations. We can couple them whenever the probability distributions of the next step have enough overlap.

3.2. Numerical algorithm

We propose the following two numerical algorithms to estimate the exponential tail of the coupling time for the rate of geometric contraction/ergodicity. Both algorithms trigger the maximal coupling when distance between the two trajectories of a coupling is smaller than a certain threshold. Since the maximal coupling should have $O(1)$ successful rate when it is

Algorithm 1. Estimate geometric rate of contraction.

Input: Initial values $x, y \in E$
Output: A lower bound of geometric rate of contraction $r > 0$
Choose threshold $d > 0$
for $i = 1$ to N **do**
  $\tau_i = 0$, $n = 0$, $(\mathcal{X}_n, \mathcal{Y}_n) = (x, y)$
  Flag $= 0$
  while Flag $= 0$ **do**
    if $|\mathcal{X}_n - \mathcal{Y}_n| > d$ **then**
      Compute $(\mathcal{X}_{n+1}, \mathcal{Y}_{n+1})$ using reflection coupling, synchronous coupling, or independent coupling
      $n \leftarrow n + 1$
    else
      Compute $(\mathcal{X}_{n+1}, \mathcal{Y}_{n+1})$ using maximal coupling
      if $\zeta_n^1 = \zeta_n^2 \sim \nu_{x,y}$ **then**
        Flag $= 1$
        $\tau_i = n$
      else
        $n \leftarrow n + 1$
      end if
    end if
  end while
end for
Use $\tau_1, \ldots, \tau_N$ to compute $\mathbb{P}[\tau > n]$
Fit log $\mathbb{P}[\tau > n]$ versus n by a linear function. Compute the slope $-r$.

triggered, the threshold d in algorithms 1 and 2 should be proportional to the standard deviation of distribution for the next step. The input of algorithm 1 is a pair of initial points (x, y), and the output is a lower bound of the geometric contraction rate of $\|P^n(x, \cdot) - P^n(y, \cdot)\|_{\mathrm{TV}}$. Algorithm 2 takes input of a point $x \in E$, and produces a lower bound of the convergence rate of $\|P^n(x, \cdot) - \pi\|_{\mathrm{TV}}$. In algorithm 2, we need to sample from the invariant probability measure. This is done by choosing the initial value of $\mathcal{Y}_0$ from a long trajectory of X_n, such that $\mathcal{Y}_0$ is approximately sampled from the invariant distribution π.

Throughout this paper, coupling time distributions in the numerical examples are plotted in the log-linear plots with powers of 10; while the slope of an exponential tail is computed by fitting log $\mathbb{P}[\tau_c > n]$ versus n with a linear function. Hence the slope of the coupling time distribution curves equals $(\log 10)^{-1}$ times the corresponding output of algorithms 1 or 2.

Since the geometric ergodicity implies the geometric contraction, in practice, it is sufficient only to run the algorithm 2 to detect the rate of geometric convergence/contraction if the sampling from π is possible. Algorithm 2 does not work well if the convergence rate is too slow for a practical long time trajectory to accurately represent samples from π. Theoretically, one can still run algorithm 1 in this situation to get the geometric contraction rate. However, a slow geometric convergence rate usually means the geometric contraction rate is slow as well, which also affects the implementation of algorithm 1.

It remains to discuss the implementation of the maximal coupling. If the probability density function of both $\mathcal{X}_{n+1}$ and $\mathcal{Y}_{n+1}$ can be explicitly given, denoted by $p^{(x)}(z)$ and $p^{(y)}(z)$ respectively, one can perform the maximal coupling by comparing these two probability density functions. We adopt the algorithm introduced in [28, 30]. See algorithm 3 for the implementation details.

Algorithm 2. Estimate convergence rate to π.

Input: Initial values $x \in E$
Output: A lower bound of convergence rate $r > 0$ to π
Choose a threshold $d > 0$, another initial point $y \in E$, and a time step size H
Let $y_0 = y$
for $i = 1$ to N **do**
  Let $X_0 = y_{i-1}$. Simulate X_t for time H
  $y_i \leftarrow X_H$
  $\tau_i = 0$, $n = 0$, $(\mathcal{X}_n, \mathcal{Y}_n) = (x, y_i)$
  Flag $= 0$
  while Flag $= 0$ **do**
    if $|\mathcal{X}_n - \mathcal{Y}_n| > d$ **then**
      Compute $(\mathcal{X}_{n+1}, \mathcal{Y}_{n+1})$ using reflection coupling, synchronous coupling, or independent coupling
      $n \leftarrow n + 1$
    else
      Compute $(\mathcal{X}_{n+1}, \mathcal{Y}_{n+1})$ using maximal coupling
      if $\zeta_n^1 = \zeta_n^2 \sim \nu_{x,y}$ **then**
        Flag $= 1$
        $\tau_i = n$
      else
        $n \leftarrow n + 1$
      end if
    end if
  end while
end for
Use $\tau_1, \ldots, \tau_N$ to compute $\mathbb{P}[\tau > n]$
Fit log $\mathbb{P}[\tau > n]$ versus n by a linear function. Compute the slope $-r$.

Algorithm 3. Maximal coupling.

Input: $(\mathcal{X}_t, \mathcal{Y}_t)$
Output: $(\mathcal{X}_{t+1}, \mathcal{Y}_{t+1})$, and τ_c if coupling is successful.
Compute probability density functions $p^{(x)}(z)$ and $p^{(y)}(z)$.
Sample $\mathcal{X}_{t+1}$ and calculate $W = Up^{(x)}(\mathcal{X}_{t+1})$, where U is a uniform random variable on $(0, 1)$.
if $W \leqslant p^{(y)}(\mathcal{X}_{t+1})$ **then**
  $\mathcal{Y}_{t+1} = \mathcal{X}_{t+1}$, $\tau_c = t + 1$
else
  Sample $\mathcal{Y}_{t+1}$ and calculate $W' = Vp^{(y)}(\mathcal{Y}_{t+1})$, where V is a uniform random variable on $(0, 1)$.
  while $W' \leqslant p^{(x)}(\mathcal{Y}_{t+1})$ **do**
    Resample $\mathcal{Y}_{t+1}$ and V. Recalculate $W' = Vp^{(y)}(\mathcal{Y}_{t+1})$.
  end while
  τ_c is still undetermined.
end if

3.3. Some remarks

As discussed in section 2.2, the reflection/synchronous coupling does not give an irreducible process in general, and we use a mixture of independent coupling and reflection/synchronous coupling so that the coupling has 'independent components'. To achieve this, at each step,

we generate an i.i.d. Bernoulli random variable Γ with $\mathbb{P}[\Gamma = 1] = \beta > 0$, which is independent of everything else. The independent coupling is chosen whenever $\Gamma = 1$, and we use the reflection/synchronous coupling for otherwise. It then follows from lemmas 2.3 and 2.4 that the exponential tail of the coupling time can be generalized to almost every initial values. It is difficult to rigorously prove the effect of β. Our numerical simulation result (see section 5.3) shows that a smaller β often corresponds to a higher convergence rate because the reflection coupling is more efficient.

In practice, for all the examples we have tested and all the couplings we have used, the exponential tails starting from different initial values have the same rate. We believe that the requirement of the independent components is only a technical limitation. Lemmas 2.3 and 2.4 should hold true for a very general class of irreducible Markov processes and couplings.

4. Geometric ergodicity of time-discrete stochastic dynamics

It has been observed that for qualitatively different deterministic dynamical systems, their small random perturbations also have qualitatively different asymptotic behaviours [40]. In this section, we numerically perform four examples of random perturbations of deterministic maps on $\mathbb{S}^1$ with distinct chaotic behaviours: (1) a uniformly expanding map; (2) an (almost) expanding map admitting a neutral fixed point; (3) an irrational rotation; (4) a logistic map with a stable periodic orbit. We note that the complexity of dynamics is decreasing from (1)–(4). For random perturbations of the above four dynamics, the geometric convergence rates are computed and compared under different noise magnitudes. Qualitative changes of the geometric convergence rates versus noises are observed. In general, as noise vanishes, the geometric convergence rate decreases in a slower way as the complexity of the underlying deterministic dynamics increases. Heuristic explanations of such changes are provided.

4.1. Expanding circle maps

Consider a deterministic dynamics given by the iterative mapping $f : \mathbb{S}^1 \to \mathbb{S}^1$:

$$f(x) = 2x + a \ \sin(2\pi x) \,(\mathrm{mod}\, 1).$$

Note that for $a < 1/(2\pi)$, f is uniformly expanding (i.e., $|f'| \geqslant 2(1 - \pi a) > 1$). It has been known that the uniformly expanding map is exponentially mixing with respect to an invariant probability measure with smooth density; see, for instance, [51].

Consider the Markov process $\boldsymbol{X}$ given by the random perturbation of f as follows

$$X_{n+1} = f(X_n) + \epsilon\zeta_n \,(\mathrm{mod}\, 1), \tag{4.1}$$

where $\{\zeta_n\}$ are i.i.d. standard normal random variables, and ϵ is the noise magnitude. In our simulations, we run algorithm 2 with $N = 10^8$ samples and collect the coupling times. For all the examples throughout this section, the threshold d of triggering the maximal coupling is set as 2ϵ because $\epsilon\zeta_t$ has a standard deviation ϵ. When the maximal coupling is triggered, we compare the probability density function on the line $\mathbb{R}$ and then fold back to $\mathbb{S}^1$. Theoretically, this is smaller than the 'true maximal coupling' for which the coupling probability should add up all the periodic images. However, it makes little difference here since $\epsilon \ll 1$.

In figure 1, the $\mathbb{P}[\tau_c > n]$ versus n plots are demonstrated in the log-linear plot, where the noise magnitudes ϵ are chosen to be 0.01, 0.02, 0.04, 0.06, 0.08, 0.1 and 0.12, respectively. We see that the coupling time distribution has exponential tails which gives the rate of geometric ergodicity. Slopes of those exponential tails are obtained by fitting log $\mathbb{P}[\tau_c > n]$ versus n using

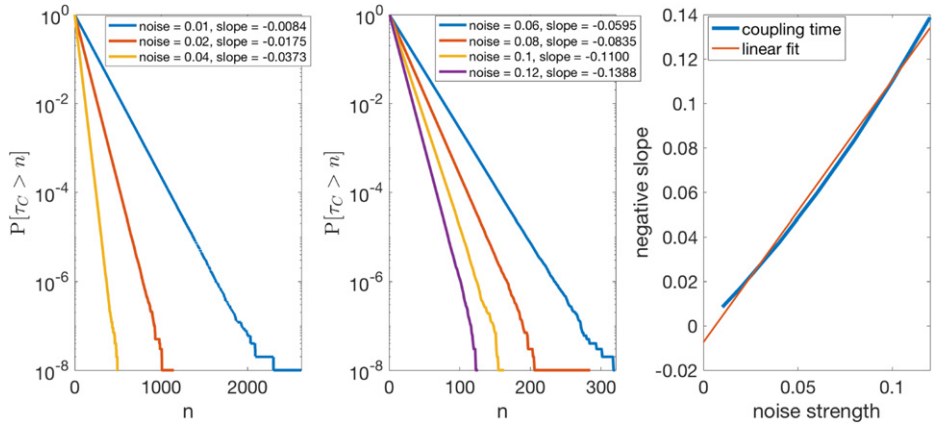

Figure 1. Example in section 4.1. Left and middle: the $\mathbb{P}[\tau_c > n]$ vs n with different noise magnitudes. Right: the negative slope of the exponential tail vs noise magnitudes, and the linear fit.

a linear function. The negative slope of the exponential tails versus ϵ is demonstrated in the lower right panel of figure 1). It drop linearly with respect to the noise magnitude. (Note that the log-linear plot uses the logarithm with base 10. Hence, the slopes of curves in figure 1 Left and Middle are the corresponding outputs of algorithm 2 multiplied by $(\log 10)^{-1}$. This applies to all numerical examples in this paper.) This is expected because the threshold to trigger the maximal coupling is 2ϵ. Two trajectories need to be $O(\epsilon)$-close in order to couple. If we assume that the trajectory of f is well-mixed, heuristically two trajectories should take $O(\epsilon^{-1})$ time to be $O(\epsilon)$ close to each other.

4.2. Circle maps with neutral fixed point

The second example is a circle map with a neutral fixed point. Consider

$$f(x) = \begin{cases} x + 2^{\alpha} x^{1+\alpha}, & 0 \leqslant x \leqslant \dfrac{1}{2}; \\ 2x - 1, & \dfrac{1}{2} < x < 1, \end{cases}$$

where $0 < \alpha < 1$ is a parameter. Note that $|f'| \geqslant 1$ on $[0, 1]$, and $|f'| = 1$ is achieved only at $x = 0$, i.e., $x = 0$ is the (unique) neutral fixed point. Thus, f is not necessarily exponentially mixing. In fact, it has been shown that in this example, f has the power-law mixing rate $n^{1-1/\alpha}$ [55].

Now, we consider the small random perturbation of f given by the Markov process $\boldsymbol{X}$ as follows

$$X_{n+1} = f(X_n) + \epsilon\zeta_n \,(\mathrm{mod}\, 1),$$

where $\{\zeta_n\}$ are i.i.d. standard normal random variables. Still, we run algorithm 2 with $N = 10^8$ samples and collect all the coupling times to compute the rate of geometric ergodicity. Noise magnitudes ϵ are chosen the same as in section 4.1. The $\mathbb{P}[\tau_c > n]$ versus n are demonstrate in the log-linear plot in figure 2 (the left and middle panel). We see that the coupling time distribution still admits exponential tails, the slope of which versus ϵ is computed and plotted

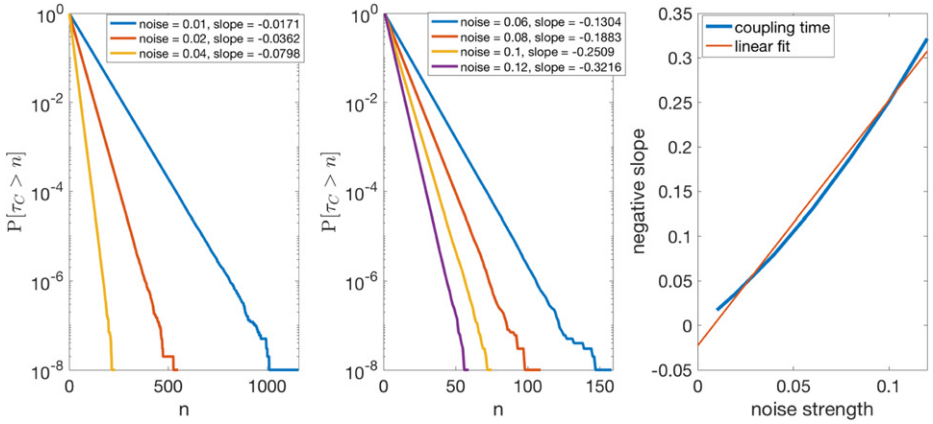

Figure 2. Example in section 4.2. Left and middle: $\mathbb{P}[\tau_c > n]$ vs n with different noise magnitudes. Right: the negative slope of the exponential tail vs noise magnitudes, and the linear fit.

in figure 2 (the right panel). Note that despite a slower mixing rate (polynomial) of f, the slope of the exponential tail still drops linearly with respect to the noise magnitude, which is same as the exponential mixing example in section 4.1. This is because the slow mixing of f is due to a longer return time from the very small neighbourhood of the unique neutral fixed point $x = 0$. A very small noise is already sufficient to 'shake' the trajectories away from the neutral fixed point to maintain a suitable mixing rate. Hence, the effect of slower-mixing rate is hard to be observed unless the noise term becomes extremely small. We refer to [5, 6] for more recent theoretical results of similar maps with very small random perturbation.

4.3. Irrational rotation (quasi-periodic)

The third example is the irrational rotation on $\mathbb{S}^1$

$$f(x) = x + \sqrt{2} \,(\mathrm{mod}\, 1). \tag{4.2}$$

Distinct from the previous two examples, for the irrational rotation (4.2), there is NO any stretching for the map f (since $|f'| \equiv 1$). Also, every orbit of f is dense going almost everywhere on $\mathbb{S}^1$. Thus, f is ergodic but not mixing.

Now, we consider the Markov process $\boldsymbol{X}$ given by

$$X_{n+1} = f(X_n) + \epsilon\zeta_n \,(\mathrm{mod}\, 1),$$

where $\{\zeta_n\}$ are i.i.d. standard normal random variables. Still, the rate of geometric ergodicity are computed by running algorithm 2 with $N = 10^8$ samples under different noise magnitudes (Here, ϵ are chosen the same as the previous two examples). The $\mathbb{P}[\tau_c > n]$ versus n plots are demonstrated in the log-linear plot in figure 3. We see that the coupling time distributions still exhibit exponential tails as the previous two examples. However, in this example, the slope (of the exponential tail) versus ϵ curve drops super-linearly, instead of linearly as in the previous two examples, as the noise magnitude decreases. We fit it by a quadratic polynomial function fairly well; see the right panel in figure 3. The heuristic reason for the $O(\epsilon^2)$ slope is the following. Without mixing, the only force that brings two trajectories together is the diffusion,

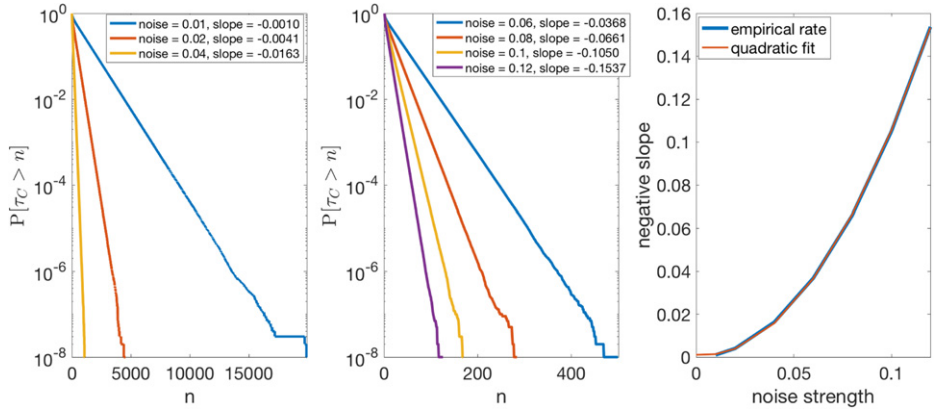

Figure 3. Example in section 4.3. Left and middle: $\mathbb{P}[\tau_c > n]$ vs n with different noise magnitudes. Right: the negative slope of the exponential tail vs noise magnitudes, and the quadratic fit.

which takes $O(\epsilon^{-2})$ time to move $O(1)$ distance. Hence, one can expect two trajectories to be 'well mixed' after $O(\epsilon^{-2})$ time.

4.4. Logistic map with stable periodic orbit

The last example is from the logistic family

$$f_\lambda = \lambda x(1-x) (\mathrm{mod}\, 1)$$

where $0 \leqslant \lambda \leqslant 4$. The logistic map was introduced as a demographic model [3] and has been well studied since then for its manipulability and abundant dynamical phenomena. It has been known that for λ between 2 and 3.569 95 (approximately), the dynamics of f_λ is simple. There is a periodic orbit, for which the period doubles as λ increases, attracting all the other trajectories. However, for a typical λ beyond the critical value 3.5699, the dynamics of f_λ goes into a chaotic regime. Any two trajectories will diverge no matter how close initially they are. In this example, we choose the logistic map

$$f := f_{3.2} = 3.2x(1-x) (\mathrm{mod}\, 1).$$

which admits a 2-periodic orbit $PQPQPQ\ldots$, where $P = 0.7995, Q = 0.5130$ (approximately), that attracts all the initial values in $(0, 1)$.

Now, we consider the Markov chain $\boldsymbol{X}$

$$X_{n+1} = f(X_n) + \epsilon\zeta_n \,(\mathrm{mod}\, 1),$$

where $\{\zeta_n\}$ are i.i.d. standard normal random variables. Still, we compute the rate of geometric ergodicity of $\boldsymbol{X}$ with different noise magnitudes by running algorithm 2 with $N = 10^8$ samples trajectories. A little bit different from the previous three examples, the noise magnitudes in this example are chosen as 0.015, 0.02, 0.03, 0.04, 0.06, 0.08, and 0.1, respectively. This is because in this example, the coupling is extremely slow which is hard to be observed numerically if the noise is too small. Slopes of the exponential tails of the coupling times are computed and demonstrated in figure 4 (blue lines). The lower right panel in figure 4 shows that the coupling becomes exponentially slow as the noise vanishes. This is because the trajectories start from

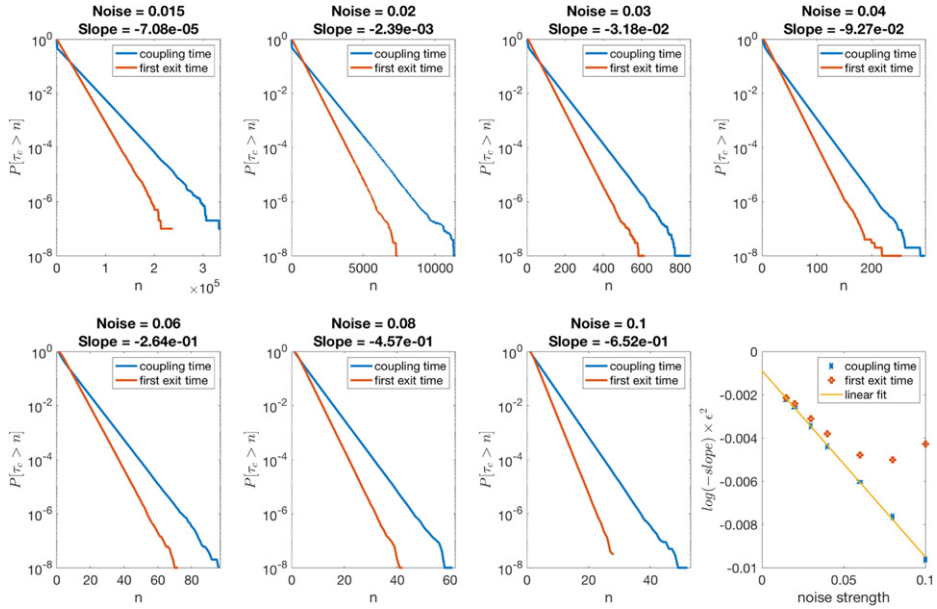

Figure 4. Example in section 4.4. First 7 panels: blue line: $\mathbb{P}[\tau_c > n]$ vs n with different noise magnitudes. Red line: log $\mathbb{P}[\eta_{PQ} > n]$ vs n with different noise magnitudes. Lower right panel: linear extrapolation of $\epsilon^2 \log(-S(\epsilon))$ and $\epsilon^2 \log(-\hat{S}(\epsilon))$, where $S(\epsilon)$ and $\hat{S}(\epsilon)$ are the slopes of exponential tail of the coupling time and the first exit time with respect to the noise magnitude ϵ, respectively.

the basin of the different periodic sequences $PQPQP\ldots$ and $QPQPQ\ldots$ need to 'overcome the attraction' from the corresponding periodic sequence in order to meet.

In addition to the lower bound, for this example, we also compute the upper bound of the rate of geometric ergodicity through the first exit time. By transparent calculations, one finds that the basin of attraction of the periodic sequences $PQPQPQ\ldots$ and $QPQPQP\ldots$ are

$$A = [0.110\,,\,0.312] \cup [0.688\,,\,0.890] \cup \cdots \quad \text{and} \quad B = [0.313\,,\,0.688] \cup \cdots,$$

respectively, i.e., a deterministic trajectory starts from A converges to the periodic sequence $PQPQPQ\ldots$, and a deterministic trajectory starts from B converges to the periodic sequence $QPQPQP\ldots$. For each value of ϵ chosen above, we compute the first exit time η_{PQ} of the coupling $(\boldsymbol{X}, \boldsymbol{Y})$ starting from $A \times B$ as follows

$$\eta_{PQ} = \min\left\{ \inf_{n\geqslant 0}\{n \mid \mathcal{X}_n \notin A, n \text{ even}, \text{or } \mathcal{X}_n \notin B, n \text{ odd}\}, \right.$$
$$\left. \inf_{n\geqslant 0}\{n \mid \mathcal{Y}_n \notin B, n \text{ even}, \text{or } \mathcal{Y}_n \notin A, n \text{ odd}\} \right\}.$$

The log-linear plots of $\mathbb{P}[\eta_{PQ} > n]$ versus n are also demonstrated in figure 4 (red lines). Still, we run 10^8 samples. We see that when ϵ is small, the distribution of the first exit time is also exponentially small as the coupling times. By proposition 2.7, this gives an upper bound for the rate of geometric ergodicity.

If let $S(\epsilon)$ and $\hat{S}(\epsilon)$ be the slopes of the exponential tails of the coupling time and first exit time under the ϵ-noise perturbation, then the large deviation theory tells that $\epsilon^2 \log(-\hat{S}(\epsilon))$

converges to a finite limit as ϵ vanishes [20]. This is confirmed by our numerical simulations in figure 4 lower right (red crosses). In addition, the term $\epsilon^2 \log(-S(\epsilon))$ also converges to a finite limit as well (blue dots).

5. Geometric ergodicity of SDEs

5.1. Numerical and analytical coupling times

For SDEs, the first issue to address is the impact of numerical approximations. As we know, the numerical trajectories $\bar{X}_t$ of an SDE are only approximations of the true trajectories X_t. Although the independent/synchronous/reflection coupling methods introduced in section 3.1 can be analogously applied to the SDE setting (2.10), the analytical coupling mechanisms are different from the numerical ones. Two trajectories of X_t are coupled whenever they meet, without the need to trigger a maximal coupling one step earlier. Such a difference makes the direct comparison of coupling times between X_t and $\bar{X}_t$ difficult, if not impossible. To solve this, for the time-h sample chain of the true SDE, we apply the numerical coupling strategy as well, i.e., the maximal coupling is triggered when two trajectories are close to each other. This enables us to compare the coupling times under the same coupling mechanisms.

Now, applying the coupling strategy in algorithm 1, we construct a coupling $(\boldsymbol{X}^h, \boldsymbol{Y}^h)$ of the time-h chain of (2.10) as follows:

(a) When the maximal coupling is not triggered, $(\mathcal{X}_n^h, \mathcal{Y}_n^h)$ evolves according to the same coupling method (independent, reflection, or synchronous) as the one used by the numerical coupling $(\bar{\mathcal{X}}_n^h, \bar{\mathcal{Y}}_n^h)$ for $n = 0, 1, \ldots$;

(b) At each $t = nh, n \geqslant 0$, check the distance between $\mathcal{X}_n^h$ and $\mathcal{Y}_n^h$. Trigger the maximal coupling if and only if $|\mathcal{X}_n^h - \mathcal{Y}_n^h| < d$, where d is the same threshold as in algorithm 1;

(c) If the maximal coupling is triggered at $t = nh$, perform the maximal coupling with respect to the probability distribution of $\mathcal{X}_{(n+1)}^h$ and $\mathcal{Y}_{(n+1)}^h$, respectively[3].

It is easy to see that $(\boldsymbol{X}^h, \boldsymbol{Y}^h)$ is a coupling of the time-h sample chain of the SDE (2.10). We further assume the following for $(\boldsymbol{X}^h, \boldsymbol{Y}^h)$ and $(\bar{\boldsymbol{X}}^h, \bar{\boldsymbol{Y}}^h)$, respectively.

(S1) The numerical scheme used in algorithm 1 is a strong approximation. More precisely, for any finite $t > 0$, there exists a constant $C(t) > 0$ such that

$$\mathbb{P}[|\bar{X}_i^h - X_i^h| > h^p] \leqslant C(t)h^{1+\alpha}, \quad i = 0, 1, \ldots, \lfloor t/h \rfloor + 1$$

holds for some $p > 1/2$, $\alpha > 0$, and all sufficiently small $h > 0$;

(S2) For each $\boldsymbol{z} := \boldsymbol{x} - \boldsymbol{y}$, the probability density function of $Z := \mathcal{X}_1^h - \mathcal{Y}_1^h$ (resp. $\bar{Z} := \bar{\mathcal{X}}_1^h - \bar{\mathcal{Y}}_1^h$) given $\mathcal{X}_0^h = \boldsymbol{x}, \mathcal{Y}_0^h = \boldsymbol{y}$ (resp. $\bar{\mathcal{X}}_0^h = \boldsymbol{x}, \bar{\mathcal{Y}}_0^h = \boldsymbol{y}$), denoted by $p_z(Z)$ (resp. $\bar{p}_z(\bar{Z})$), satisfies

$$C_b h^{-k/2} \mathrm{e}^{-(Z-z)^\top \Sigma_b (Z-z)/h} \leqslant p_z(Z) \leqslant C_u h^{-k/2} \mathrm{e}^{-(Z-z)^\top \Sigma_u (Z-z)/h}$$

$$\left(\text{resp. } \bar{C}_b h^{-k/2} \mathrm{e}^{-(\bar{Z}-z)^\top \bar{\Sigma}_b (\bar{Z}-z)/h} \leqslant \bar{p}_z(\bar{Z}) \leqslant \bar{C}_u h^{-k/2} \mathrm{e}^{-(\bar{Z}-z)^\top \bar{\Sigma}_u (\bar{Z}-z)/h}\right),$$

[3] If at step (ii), we already have $\mathcal{X}_n^h = \mathcal{Y}_n^h$. Then we just set $\tau_c = nh$, and the step (iii) will not be implemented. However, for strong Feller processes, this happens with zero probability.

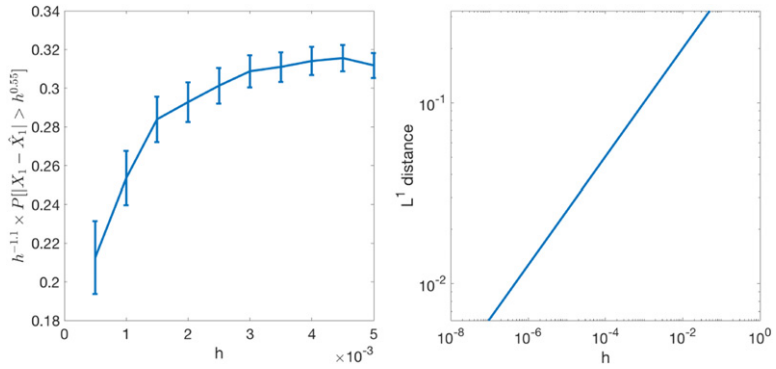

Figure 5. Left: $\mathbb{P}[|\bar{X}_1 - X_1| > h^{0.55}]/h^{1.1}$ for different h, where X_t is a geometric Brownian motion. Error bars are included. Right: L^1 distance between the probability density function of $N(0, h)$ and that of $N(h^{0.8}, h)$ for different small h.

where Σ_u, Σ_b (resp.$\bar{\Sigma}_u, \bar{\Sigma}_b$) are positive definite $k \times k$ matrices, and $C_u, C_b > 0$ (resp. $\bar{C}_u, \bar{C}_b > 0$) are constants in order $O(1)$;

(S3) The threshold d to trigger the maximal coupling is in order $O(\sqrt{h})$. To be specific, we set $d = 2\epsilon\sqrt{h}$, where ϵ is the noise magnitude in (2.10);

(S4) The probability density function of X_1^h (resp. $\bar{X}_1^h$) conditioning on $X_0^h = \boldsymbol{x}$ (resp. $\bar{X}_0^h = \boldsymbol{x}$), denoted by $f_{\boldsymbol{x}}^h$ (resp. $\bar{f}_{\boldsymbol{x}}^h$), changes continuously with respect to h. More precisely, there exists a function $\varphi : \mathbb{R}_+ \to \mathbb{R}_+$ satisfying $\lim_{h\to 0} \varphi(h) = 0$ such that for all $\gamma > 1/2$ and the unit vector $\boldsymbol{v} \in \mathbb{R}^k$, it holds that

$$\|f_{\boldsymbol{x}}^h - f_{\boldsymbol{x}+h^\gamma \boldsymbol{v}}^h\|_{L^1} < \varphi(h) \quad (\text{resp. } \|\bar{f}_{\boldsymbol{x}}^h - \bar{f}_{\boldsymbol{x}+h^\gamma \boldsymbol{v}}^h\|_{L^1} < \varphi(h)).$$

In addition, the one-step transition probability density function $\bar{f}_{\boldsymbol{x}}^h$ approximates $f_{\boldsymbol{x}}^h$ in the L^1-norm, i.e.,

$$\|f_{\boldsymbol{x}}^h - \bar{f}_{\boldsymbol{x}}^h\|_{L^1} < \varphi(h), \quad \forall\, \boldsymbol{x} \in \mathbb{R}^k.$$

Also, we require that the two coupling processes $(\mathcal{X}_t, \mathcal{Y}_t)$ and $(\bar{\mathcal{X}}_t, \bar{\mathcal{Y}}_t)$ use the same Brownian motion as the true SDE trajectory to produce the discrete random variables. This makes the comparison between the numerical and true SDE trajectories possible.

Essentially, **(S1)**–**(S4)** assume that (i) $\bar{\boldsymbol{X}}^h$ is a strong approximation of $\boldsymbol{X}^h$ with a good control of the tails; (ii) the probability density function of X_1^h given X_0^h (resp. $\bar{X}_1^h$ given $\bar{X}_0^h$) is a good approximation of a Gaussian function with variance $O(h)$. We justify the assumptions **(S1)**–**(S4)** by numerical computations or the theoretical arguments. Please see the following remark 5.1.

Remark 5.1. Assumptions **(S2)** and **(S4)** are both about the transition probability density function. When the Euler–Maruyama scheme is used, $\bar{p}_z$ and $\bar{f}_{\boldsymbol{x}}^h$ are probability density functions of normal distributions, and for h sufficiently small, p_z and $f_{\boldsymbol{x}}^h$ are also closely approximated by the normal probability density functions. Hence, **(S2)** and **(S4)** are reasonable assumptions. In particularly, if g and σ in (2.10) are constants, **(S2)** holds easily, as well as the first inequality in **(S4)**. For the second inequality in **(S4)**, it is not easy to integrate $|\bar{f}_{\boldsymbol{x}}^h - \bar{f}_{\boldsymbol{x}+h^\gamma \boldsymbol{v}}^h|$ by hand, which is equivalent to integrating

$$\int_{\mathbb{R}^d} (2\pi)^{-d/2} \det(h\Sigma)^{-1/2} |\mathrm{e}^{-\boldsymbol{x}^T (h\Sigma)^{-1} \boldsymbol{x}/2} - \mathrm{e}^{-(\boldsymbol{x}-h^\gamma \boldsymbol{v})^T (h\Sigma)^{-1} (\boldsymbol{x}-h^\gamma \boldsymbol{v})/2}| \,\mathrm{d}\boldsymbol{x},$$

where $\Sigma = \sigma(\boldsymbol{x})$. We numerically compute the L^1 distance between the probability density function of $N(0,h)$ and $N(h^{0.8},h)$ for different small h, and plotted in figure 5 left. The L^1 distance converges to zero at a power-law speed with respect to h. This verifies **(S4)**.

For **(S1)**, we numerically compare the strong error of Milstein scheme for the geometric Brownian motion $\mathrm{d}X_t = 0.2X_t\mathrm{d}t + X_t\mathrm{d}W_t$ at $t=1$. The ratio $\mathbb{P}[|\bar{X}_1 - X_1| > h^{0.55}]/h^{1.1}$ for different h is plotted in figure 5 left. We see that the ratio decreases with respect to h. Hence **(S1)** is satisfied.

In practice, the threshold d in **(S3)** can be set as $d = C\sqrt{h}$ with C being in the same scale as ϵ (here, we choose $C = 2\epsilon$). In this way, the two trajectories can be coupled with certain reasonable probability once the maximal coupling is triggered. Our numerical study finds that the numerical coupling time is not very sensitive against C.

Theorem 5.2. *Let τ_c and $\bar{\tau}_c$ be the coupling times of $(\boldsymbol{X},\boldsymbol{Y})$ and $(\bar{\boldsymbol{X}},\bar{\boldsymbol{Y}})$, respectively. Assume that* **(S1)**–**(S4)** *hold. Then for any finite $t>0$, there exists $a(t)>0$ such that for any $b \in (0, p-\frac{1}{2})$ and any $h>0$ sufficiently small, it holds that*

$$|\mathbb{P}[\tau_c > t] - \mathbb{P}[\bar{\tau}_c > t]| \leqslant a(t)h^{\alpha} + c\varphi(h) + h^{p-\frac{1}{2}-b}, \tag{5.1}$$

where $c>0$ is a uniform constant for all small $h>0$, and the parameters α, p are as in **(S1)**. In particularly,

$$\lim_{h\to 0} \mathbb{P}[\bar{\tau}_c > t] = \mathbb{P}[\tau_c > t].$$

By theorem 5.2, if an extrapolation of small h shows that the exponential tail of the coupling time of $(\bar{\boldsymbol{X}}^h, \bar{\boldsymbol{Y}}^h)$ is strictly away from zero, then the numerical coupling provides a lower bound of the geometric convergence/contraction rate of the SDE (2.10).

In the remainder of this section we prove theorem 5.2. Before proceeding to the proof, we briefly describe the idea of it. Observe that at each step i, if the coupling succeeds for $(\mathcal{X}_i^h, \mathcal{Y}_i^h)$, then at the previous step $(i-1)$, $\mathcal{X}_{i-1}^h$ and $\mathcal{Y}_{i-1}^h$ must be sufficiently close so that the maximal coupling is triggered. The strong approximation property **(S1)** then guarantees that at the step $(i-1)$, very likely, the maximal coupling is also triggered for the numerical coupling $(\bar{\mathcal{X}}_n^h, \bar{\mathcal{Y}}_n^h)$. In other words, the maximal coupling is triggered for one coupling process while not for the other can only happen with small probability. The events $\mathscr{A}_{i-1}$, $\bar{\mathscr{A}}_{i-1}$, $\mathscr{B}_{i-1}$ and $\mathscr{C}_{i-1}$ defined below as well as proposition 5.3 are to indicate this. Moreover, whenever the maximal coupling is triggered, as long as $\mathcal{X}_{i-1}^h, \bar{\mathcal{X}}_{i-1}^h$ and $\mathcal{Y}_{i-1}^h, \bar{\mathcal{Y}}_{i-1}^h$ are both close, the probabilities to achieve a successful coupling at the next step are about the same. Lemma 5.4 is to establish this. Although there are situations when $|\mathcal{X}_n^h - \mathcal{Y}_n^h|$ (resp. $|\bar{\mathcal{X}}_n^h - \bar{\mathcal{Y}}_n^h|$) falls at the 'edge' of the triggering area, the probabilities are small as stated by lemma 5.5.

Proof of Theorem 5.2. For convenience, write $t = n_h h$ where $n_h = \lceil \frac{t}{h} \rceil$. Recall that we use n_c (resp. $\bar{n}_c$) to denote the numerical steps for a successful coupling for the time-h chain $\boldsymbol{X}^h$ (resp. $\bar{\boldsymbol{X}}^h$), where $\tau_c = hn_c$ (resp. $\bar{\tau}_c = h\bar{n}_c$). Then

$$|\mathbb{P}[\tau_c > t] - \mathbb{P}[\bar{\tau}_c > t]| = |\mathbb{P}[n_c > n_h] - \mathbb{P}[\bar{n}_c > n_h]| = |\mathbb{P}[n_c \leqslant n_h] - \mathbb{P}[\bar{n}_c \leqslant n_h]|.$$

Since the maximal coupling is triggered no early than the second step, we have

$$|\mathbb{P}[n_c \leqslant n_h] - \mathbb{P}[\bar{n}_c \leqslant n_h]| \leqslant \sum_{i=2}^{n_h} |\mathbb{P}[n_c = i] - \mathbb{P}[\bar{n}_c = i]|.$$

As discussed above, for each $2 \leqslant i \leqslant n_h$, if the coupling between $\bar{\mathcal{X}}_n^h$ and $\bar{\mathcal{Y}}_n^h$ occurs at step i, then at step $(i-1)$, besides that the maximal coupling of $(\mathcal{X}_n^h, \mathcal{Y}_n^h)$ must be triggered, the maximal coupling of $(\bar{\mathcal{X}}_n^h, \bar{\mathcal{Y}}_n^h)$ is (very likely) triggered as well. To clarify this, we split each

term ($\mathbb{P}[n_c = i] - \mathbb{P}[\bar{n}_c = i]$) according to whether the coupling process at the step $(i-1)$ falls at the 'edge' of the triggering area. The following several events are defined according to this. Fix $\delta \in (0, \frac{p-\frac{1}{2}}{3})$. Let

$$\mathscr{A}_{i-1} = \left\{ |\mathcal{X}^h_{i-1} - \mathcal{Y}^h_{i-1}| < d - h^{p-\delta}, n_c > i-1 \right\},$$

$$\bar{\mathscr{A}}_{i-1} = \left\{ |\bar{\mathcal{X}}^h_{i-1} - \mathcal{Y}^h_{i-1}| < d - h^{p-\delta}, \bar{n}_c > i-1 \right\},$$

$$\mathscr{B}_{i-1} = \left\{ |\bar{\mathcal{X}}^h_{i-1} - \mathcal{X}^h_{i-1}| \leqslant \frac{1}{2}h^{p-\delta}, |\bar{\mathcal{Y}}^h_{i-1} - \mathcal{Y}^h_{i-1}| \leqslant \frac{1}{2}h^{p-\delta}, n_c > i-1, \bar{n}_c > i-1 \right\},$$

$$\begin{aligned}\mathscr{C}_{i-1} = \Bigg\{ & |\mathcal{X}^h_{i-1} - \mathcal{Y}^h_{i-1}| < d, |\bar{\mathcal{X}}^h_{i-1} - \mathcal{Y}^h_{i-1}| < d, |\bar{\mathcal{X}}^h_{i-1} - \mathcal{X}^h_{i-1}| \\ & \leqslant \frac{1}{2}h^{p-\delta}, |\bar{\mathcal{Y}}^h_{i-1} - \mathcal{Y}^h_{i-1}| \leqslant \frac{1}{2}h^{p-\delta}, n_c > i-1, \bar{n}_c > i-1 \Bigg\},\end{aligned}$$

where $p > 1/2, d = 2\epsilon\sqrt{h}$ are from **(S1)** and **(S3)**, respectively. Note that the occurrence of both events $\mathscr{A}_{i-1}$ (resp. $\bar{\mathscr{A}}_{i-1}$) and $\mathscr{B}_{i-1}$ induces the occurrence of the event $\mathscr{C}_{i-1}$, i.e.,

$$\mathscr{A}_{i-1} \backslash \mathscr{C}_{i-1} \subseteq \mathscr{B}^c_{i-1} \quad (\text{resp. } \bar{\mathscr{A}}_{i-1} \backslash \mathscr{C}_{i-1} \subseteq \mathscr{B}^c_{i-1}).$$

Combined with the strong approximation property **(S1)**, we immediately obtain the following estimates.

Proposition 5.3. *For each $2 \leqslant i \leqslant n_h$, it holds that*

$$\mathbb{P}[n_c = i, \mathscr{A}_{i-1} \backslash \mathscr{C}_{i-1}] \leqslant 2C(t)h^{1+\alpha} \text{ (resp. } \mathbb{P}[\bar{n}_c = i, \bar{\mathscr{A}}_{i-1} \backslash \mathscr{C}_{i-1}] \leqslant 2C(t)h^{1+\alpha}),$$

where $C(t)$ is from **(S1)**.

Now, for each $2 \leqslant i \leqslant n_h$, we split $\mathbb{P}[n_c = i]$ (resp. $\mathbb{P}[\bar{n}_c = i]$) as

$$\mathbb{P}[n_c = i] = \mathbb{P}[n_c = i, \mathscr{C}_{i-1}] + \mathbb{P}[n_c = i, \mathscr{A}_{i-1} \backslash \mathscr{C}_{i-1}] + \mathbb{P}[n_c = i, \mathscr{A}^c_{i-1}].$$

(resp. $\mathbb{P}[\bar{n}_c = i] = \mathbb{P}[\bar{n}_c = i, \bar{\mathscr{A}}_{i-1}] + \mathbb{P}[\bar{n}_c = i, \bar{\mathscr{A}}_{i-1} \backslash \mathscr{C}_{i-1}] + \mathbb{P}[\bar{n}_c = i, \bar{\mathscr{A}}^c_{i-1}]$).

By proposition 5.3 we have

$$\begin{aligned}|\mathbb{P}[n_c = i] - \mathbb{P}[\bar{n}_c = i]| \leqslant & |\mathbb{P}[n_c = i, \mathscr{C}_{i-1}] - \mathbb{P}[\bar{n}_c = i, \mathscr{C}_{i-1}]| + 4C(t)h^{1+\alpha} \\ & + |\mathbb{P}[n_c = i, \mathscr{A}^c_{i-1}] - \mathbb{P}[\bar{n}_c = i, \bar{\mathscr{A}}^c_{i-1}]|.\end{aligned}$$

Hence, the estimation of $|\mathbb{P}[n_c = i] - \mathbb{P}[\bar{n}_c = i]|$ is reduced to the estimations of

$$|\mathbb{P}[n_c = i, \mathscr{C}_{i-1}] - \mathbb{P}[\bar{n}_c = i, \mathscr{C}_{i-1}]|$$

and

$$|\mathbb{P}[n_c = i, \mathscr{A}^c_{i-1}] - \mathbb{P}[\bar{n}_c = i, \bar{\mathscr{A}}^c_{i-1}]|.$$

These are concluded by the following two lemmas.

Lemma 5.4. *For each $2 \leqslant i \leqslant n_h$, it holds that*

$$|\mathbb{P}[n_c = i, \mathscr{C}_{i-1}] - \mathbb{P}[\bar{n}_c = i, \mathscr{C}_{i-1}]| \leqslant c_0\varphi(h)\mathbb{P}[n_c = i],$$

where $c_0 > 0$ is a uniform constant for all i and small $h > 0$.

Lemma 5.5. *For each $2 \leqslant i \leqslant n_h$, the following hold*

$$\mathbb{P}[n_c = i, \mathscr{A}^c_{i-1}] \leqslant c_1 h^{p-\frac{1}{2}-2\delta}\mathbb{P}[n_c = i] \tag{5.2}$$

$$\mathbb{P}[\bar{n}_c = i, \bar{\mathscr{A}}^c_{i-1}] \leqslant c_1 h^{p-\frac{1}{2}-2\delta}\mathbb{P}[\bar{n}_c = i], \tag{5.3}$$

where $c_1 > 0$ is a uniform constant for all i and small $h > 0$.

We postpone the proofs of lemmas 5.4 and 5.5 to the end. Combining all the estimates above,

$$\begin{aligned}|\mathbb{P}[n_c = i] - \mathbb{P}[\bar{n}_c = i]| \leqslant\ & 4C(t)h^{1+\alpha} + c_0\varphi(h)\mathbb{P}[n_c = i] \\ & + c_1 h^{p-\frac{1}{2}-2\delta}(\mathbb{P}[n_c = i] + \mathbb{P}[\bar{n}_c = i]).\end{aligned}$$

Note that

$$\sum_{i=2}^{n_h}\mathbb{P}[n_c = i] \leqslant 1, \quad \sum_{i=2}^{n_h}\mathbb{P}[\bar{n}_c = i] \leqslant 1.$$

Then together with n_h being in the order $O(t/h)$, we finally obtain

$$\begin{aligned}\sum_{i=2}^{n_h}|\mathbb{P}[n_c = i] - \mathbb{P}[\bar{n}_c = i]| &\leqslant 4n_hC(t)h^{1+\alpha} + c_0\varphi(h)\sum_{i=2}^{n_h}\mathbb{P}[n_c = i] \\ &\quad + c_1 h^{p-\frac{1}{2}-2\delta}\sum_{i=2}^{n_h}(\mathbb{P}[n_c = i] + \mathbb{P}[\bar{n}_c = i]) \\ &\leqslant \tilde{C}(t)h^{\alpha} + c_0\varphi(h) + 2c_1h^{p-\frac{1}{2}-2\delta},\end{aligned}$$

where $\tilde{C}(t) > 0$ only depend on t.

Now, theorem 5.2 is proved by setting $a(t) = \tilde{C}(t)$ and $b = 3\delta$.

Proof of Lemma 5.4. Since $(p - \delta) > 1/2$, if denote $f_{\boldsymbol{x}}, f_{\bar{\boldsymbol{x}}}$ (resp. $f_{\boldsymbol{y}}, \bar{f}_{\bar{\boldsymbol{y}}}$) as the probability density functions of $\mathcal{X}^h_i, \bar{\mathcal{X}}^h_i$ (resp. $\mathcal{Y}^h_i, \bar{\mathcal{Y}}^h_i$) conditioning on $\mathcal{X}^h_{i-1} = \boldsymbol{x}, \bar{\mathcal{X}}^h_{i-1} = \bar{\boldsymbol{x}}$ (resp. $\mathcal{Y}^h_{i-1} = \boldsymbol{y}, \bar{\mathcal{Y}}^h_{i-1} = \bar{\boldsymbol{y}}$), by **(S4)**, we have

$$\|f_{\boldsymbol{x}} - \bar{f}_{\bar{\boldsymbol{x}}}\|_{L^1} \leqslant 2\varphi(h) \text{ (resp. } \|f_{\boldsymbol{y}} - \bar{f}_{\bar{\boldsymbol{y}}}\|_{L^1} \leqslant 2\varphi(h)).$$

Then the mechanism of the maximal coupling yields

$$\begin{aligned}|\mathbb{P}[n_c = i, \mathscr{C}_{i-1}] - \mathbb{P}[\bar{n}_c = i, \mathscr{C}_{i-1}]| &= |\mathbb{P}[n_c = i|\mathscr{C}_{i-1}] - \mathbb{P}[\bar{n}_c = i|\mathscr{C}_{i-1}]| \cdot \mathbb{P}[\mathscr{C}_{i-1}] \\ &\leqslant 4\varphi(h)\mathbb{P}[\mathscr{C}_{i-1}].\end{aligned}$$

Note that as long as the maximal coupling is triggered, the coupling probability is in order $O(1)$ and uniform with respect to all small $h > 0$, i.e.,

$$\mathbb{P}[n_c = i, \mathscr{C}_{i-1}] \geqslant \eta_0\mathbb{P}[\mathscr{C}_{i-1}]$$

for a constant $\eta_0 > 0$. Therefore,

$$|\mathbb{P}[n_c = i, \mathscr{C}_{i-1}] - \mathbb{P}[\bar{n}_c = i, \mathscr{C}_{i-1}]| \leqslant (4\varphi(h)/\eta_0)\mathbb{P}[n_c = i, \mathscr{C}_{i-1}] \leqslant (4\varphi(h)/\eta_0)\mathbb{P}[n_c = i].$$

Lemma 5.4 is proved by letting $c_0 = 4/\eta_0$.

Proof of Lemma 5.5. We only need to prove (5.2), and (5.3) can be obtained similarly. First, we estimate $\mathbb{P}[d - h^{p-\delta} \leqslant |\mathcal{X}^h_{i-1} - \mathcal{Y}^h_{i-1}| \leqslant d]$. Conditioning on the value at the step $(i-2)$, we have

$$\begin{aligned}\mathbb{P}[d - h^{p-\delta} \leqslant |\mathcal{X}^h_{i-1} - \mathcal{Y}^h_{i-1}| \leqslant d] = \int_{\mathbb{R}^k\times\mathbb{R}^k} &\mathbb{P}\left[d - h^{p-\delta} \leqslant |\mathcal{X}^h_{i-1} - \mathcal{Y}^h_{i-1}|\right.\\ &\left.\leqslant d \,|\, \mathcal{X}^h_{i-2} = \boldsymbol{x}, \mathcal{Y}^h_{i-2} = \boldsymbol{y}\right] \mu_{i-2}(\mathrm{d}\boldsymbol{x}, \mathrm{d}\boldsymbol{y}),\end{aligned}$$

where $\mu_{i-2}(\mathrm{d}\boldsymbol{x}, \mathrm{d}\boldsymbol{y})$ is the joint probability distribution of $(\mathcal{X}^h_{i-2}, \mathcal{Y}^h_{i-2})$.

By **(S2)**, the probability density function of $(\mathcal{X}^h_{i-1} - \mathcal{Y}^h_{i-1})$ conditional on $\mathcal{X}^h_{i-2} = \boldsymbol{x}, \mathcal{Y}^h_{i-2} = \boldsymbol{y}$ is Gaussian-like. So we have the following comparison of $\mathbb{P}[d - h^{p-\delta} \leqslant |\mathcal{X}^h_{i-1} - \mathcal{Y}^h_{i-1}| \leqslant d \,|\, \mathcal{X}^h_{i-2} = \boldsymbol{x}, \mathcal{Y}^h_{i-2} = \boldsymbol{y}]$ and $\mathbb{P}[|\mathcal{X}^h_{i-1} - \mathcal{Y}^h_{i-1}| \leqslant d \,|\, \mathcal{X}^h_{i-2} = \boldsymbol{x}, \mathcal{Y}^h_{i-2} = \boldsymbol{y}]$ as follows:

(a) If $|\boldsymbol{x} - \boldsymbol{y}| \leqslant -\delta \log h \cdot h^{1/2}$. Since $d = O(h^{1/2})$, within the set $\{|\mathcal{X}^h_{i-1} - \mathcal{Y}^h_{i-1}| \leqslant d\}$, the maximal density of $(\mathcal{X}^h_{i-1} - \mathcal{Y}^h_{i-1})$ is at most $O(h^{-\delta})$ times the minimal density of $(\mathcal{X}^h_{i-1} - \mathcal{Y}^h_{i-1})$. In consideration that the volume of the shell $\{(\boldsymbol{u}, \boldsymbol{w}) \in \mathbb{R}^k : d - h^{p-\delta} \leqslant |\boldsymbol{u} - \boldsymbol{w}| \leqslant d\}$ is $O(h^{(k-1)/2+p-\delta})$, we can find a constant $c > 0$ such that

$$\begin{aligned}&\mathbb{P}\left[d - h^{p-\delta} \leqslant |\mathcal{X}^h_{i-1} - \mathcal{Y}^h_{i-1}| \leqslant d \,|\, \mathcal{X}^h_{i-2} = \boldsymbol{x}, \mathcal{Y}^h_{i-2} = \boldsymbol{y}\right]\\ &\qquad\leqslant ch^{k/2+p-\frac{1}{2}-2\delta}\mathbb{P}\left[|\mathcal{X}^h_{i-1} - \mathcal{Y}^h_{i-1}| \leqslant d \,|\, \mathcal{X}^h_{i-2} = \boldsymbol{x}, \mathcal{Y}^h_{i-2} = \boldsymbol{y}\right];\end{aligned}$$

(b) If $|\boldsymbol{x} - \boldsymbol{y}| > -\delta \log h \cdot h^{1/2}$. Then the probability density of $(\mathcal{X}^h_{i-1} - \mathcal{Y}^h_{i-1})$ within the set $\{|\mathcal{X}^h_{i-1} - \mathcal{Y}^h_{i-1}| \leqslant d\}$ is less than $ce^{-(\delta \log h)^2}h^{-k/2}$ (here, we still use $c > 0$ as a uniform constant), which converges to zero faster than h^r for any $r > 0$. Hence,

$$\begin{aligned}&\mathbb{P}\left[d - h^{p-\delta} \leqslant |\mathcal{X}^h_{i-1} - \mathcal{Y}^h_{i-1}| \leqslant d \,|\, \mathcal{X}^h_{i-2} = \boldsymbol{x}, \mathcal{Y}^h_{i-2} = \boldsymbol{y}\right]\\ &\qquad\leqslant h^{p-\frac{1}{2}-\delta+r}\mathbb{P}\left[|\mathcal{X}^h_{i-1} - \mathcal{Y}^h_{i-1}| \leqslant d \,|\, \mathcal{X}^h_{i-2} = \boldsymbol{x}, \mathcal{Y}^h_{i-2} = \boldsymbol{y}\right].\end{aligned}$$

Now, for both cases, integrating over the initial conditions $(\boldsymbol{x}, \boldsymbol{y})$, we have

$$\mathbb{P}[d - h^{p-\delta} \leqslant |\mathcal{X}^h_{i-1} - \mathcal{Y}^h_{i-1}| \leqslant d] \leqslant h^{p-\frac{1}{2}-2\delta}\mathbb{P}[|\mathcal{X}^h_{i-1} - \mathcal{Y}^h_{i-1}| \leqslant d].$$

Consequently,

$$\begin{aligned}&\mathbb{P}[n_c = i, \mathscr{A}^c_{i-1}]\\ &\quad= \mathbb{P}[n_c = i | d - h^{p-\delta} \leqslant |\mathcal{X}^h_{i-1} - \mathcal{Y}^h_{i-1}| \leqslant d] \cdot \mathbb{P}[d - h^{p-\delta} \leqslant |\mathcal{X}^h_{i-1} - \mathcal{Y}^h_{i-1}| \leqslant d]\\ &\quad\leqslant h^{p-\frac{1}{2}-2\delta} \cdot \mathbb{P}[n_c = i | d - h^{p-\delta} \leqslant |\mathcal{X}^h_{i-1} - \mathcal{Y}^h_{i-1}| \leqslant d] \cdot \mathbb{P}[|\mathcal{X}^h_{i-1} - \mathcal{Y}^h_{i-1}| \leqslant d]\end{aligned}$$

As in the proof of lemma 5.4, since the coupling probability conditioning on the event $\{|\mathcal{X}^h_{i-1} - \mathcal{Y}^h_{i-1}| \leqslant d\}$ is uniform for all small $h > 0$, we have

$$\mathbb{P}[n_c = i | d - h^{p-\delta} \leqslant |\mathcal{X}^h_{i-1} - \mathcal{Y}^h_{i-1}| \leqslant d] \leqslant \mathbb{P}[n_c = i | \mathcal{X}^h_{i-1} - \mathcal{Y}^h_{i-1}| \leqslant d]/\eta_0,$$

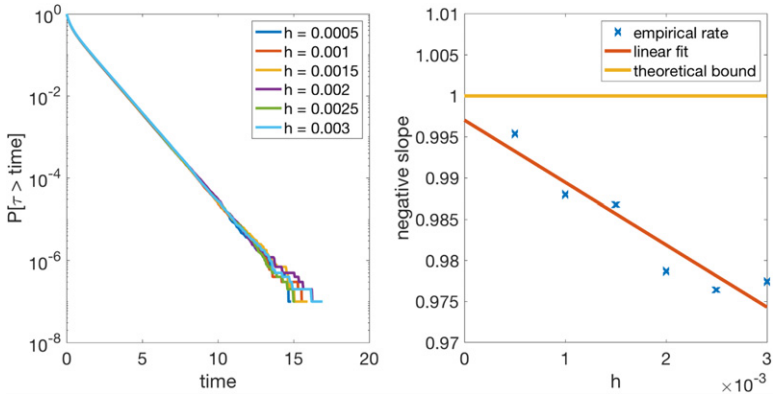

Figure 6. Left: coupling time distribution of the overdamped Langevin dynamics under different time step sizes. Right: comparison of exponential tails of coupling time with different time step sizes.

where η_0 is as in the proof of lemma 5.4. Thus,

$$\mathbb{P}[n_c = i, \mathscr{A}_{i-1}^c] \leqslant (h^{p-\frac{1}{2}-2\delta}/\eta_0)\mathbb{P}[n_c = i].$$

By setting $c_1 = 1/\eta_0$, lemma 5.5 is proved.

5.2. Overdamped Langevin dynamics

The first SDE example we shall use is the overdamped Langevin dynamics. Consider

$$\mathrm{d}X_t = -\nabla V(X_t) + \epsilon\,\mathrm{d}W_t, \tag{5.4}$$

where $V(x)$ is a potential function. It is well known that (5.4) admits a unique invariant probability measure π_ϵ with the probability density

$$\rho_\epsilon = \frac{1}{K}\mathrm{e}^{-2\,\mathrm{V}(X)/\epsilon^2},$$

where K is a normalizer. In addition, if V is strictly convex such that $\mathrm{Hess}(V) - R\mathrm{Id}_k$ is positive definite, then π_ϵ satisfies the Logarithmic Sobolev inequality with constant $\epsilon^2 R/2$. Hence, the geometric convergence rate is at least R. (We refer to [4, 37] for details.) Now we check our numerical result for the rate of geometric ergodicity with the above analytical result.

Consider $n = 2$ and $V(x, y) = (x^2 + y^2)/2$. This potential function is strictly convex with Hessian matrix Id_2. We run algorithm 2 for different steps sizes $h = 0.0005, 0.001, 0.0015, 0.002, 0.0025$ and 0.003. Throughout this section, the threshold of triggering the maximal coupling is set as $d = 2\epsilon\sqrt{h}$. The sample size $N = 10^7$. To reach the optimal coupling rate, we use the reflection coupling until the maximal coupling is triggered. Coupling time distributions versus different step sizes are compared in a log-linear plot (figure 6 left). The slopes of those exponential tails are computed by fitting $\log\ \mathbb{P}[\tau_c > t]$ versus t using a linear function. We linearly extrapolate the negative slopes for decreasing h in figure 6 right. We see that the numerical result for the rate of geometric ergodicity is very close to the theoretical one. In addition, a smaller time step size gives a higher rate. By theorem 5.2, these numerically computed rates of geometric ergodicity are trustable.

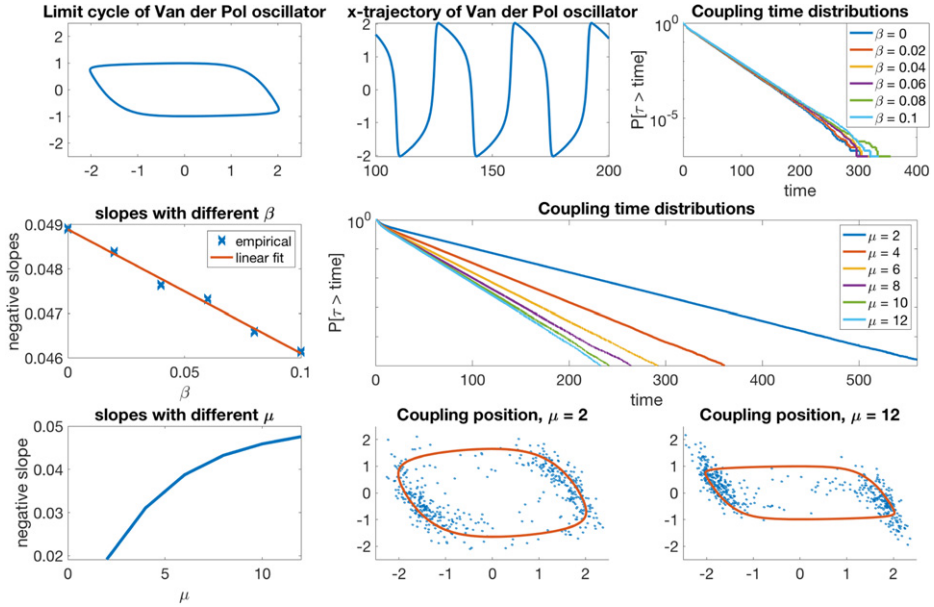

Figure 7. Top left: limit cycle of the Van der Pol oscillator for $\mu = 12$. Top mid: deterministic trajectory of x-variable. Top right: $\mathbb{P}[\tau_c > t]$ versus t for different values of β in log-linear plot. Mid left: linear fit of negative slopes of $\mathbb{P}[\tau_c > t]$ versus t for different values of β. Mid right: $\mathbb{P}[\tau_c > t]$ versus t for different values of μ in log-linear plot. Bottom left: negative slopes of $\mathbb{P}[\tau_c > t]$ versus t for different values of β. Bottom mid: positions where two trajectories couple when $\mu = 2$. Bottom right: positions where two trajectories couple when $\mu = 12$.

5.3. Van der Pol oscillator

The second SDE example is the Van der Pol oscillator with additive noise. We use this example to demonstrate the effect of slow-fast dynamics on the geometric ergodicity. Consider

$$\begin{aligned} \mathrm{d}X_t &= \left(X_t - \frac{1}{3}X_t^3 - Y_t\right)\mathrm{d}t + \epsilon\,\mathrm{d}W_t^1 \\ \mathrm{d}Y_t &= \frac{1}{\mu}X_t\,\mathrm{d}t + \epsilon\,\mathrm{d}W_t^2. \end{aligned} \tag{5.5}$$

The deterministic part of (5.5) admits a limit cycle, as shown in figure 7 top left. When $\mu \gg 1$, this system demonstrates the slow-fast dynamics, which is called the relaxation oscillation. The solution will move slowly along left/right side of the limit cycle for a long time, and then jump to the other side quickly after passing the 'folding point'. See figure 7 top middle for x-trajectory versus time of the deterministic equation.

The Van der Pol oscillator has been studied for decades. We shall use our coupling methods to numerically study the spectral property of (5.5). The magnitude of noise is chosen as $\epsilon = 0.3$, which is small compared with the size of the limit cycle. We run algorithm 2 with $N = 10^7$ samples and time step size is set as $h = 0.001$. Before the two trajectories are sufficiently close to each other, we use a mixture of the independent and reflection couplings. More precisely, at each step, with probability β we use the independent coupling, and use the reflection coupling for otherwise. This makes the coupling process irreducible. In the first simulation, we fix

$\mu = 12$ and let $\beta = 0, 0.02, 0.04, 0.06, 0.08, 0.1$. We find that the resultant rate of the exponential tails decreases slightly as β increases since the reflection coupling is more efficient than the independent coupling. However, this dependency is not very sensitive; see figure 7 top right and middle left for more details.

In the second simulation, we fix $\beta = 0.05$ and let $\mu = 2, 4, 6, 8, 10, 12$. The exponential tails of the coupling time distribution corresponding to the different μ's are compared; see figure 7 middle right and bottom left. Note that the middle right figure is cut off at the probability 10^{-5} and horizontally stretched in order to demonstrate the difference between $\mu = 10$ and $\mu = 12$ plots. The slopes of these exponential tails versus different μ's are computed and plotted in figure 7 bottom left.

In this example, the rate of geometric ergodicity is small. This is expected because one trajectory needs to diffuse along the limit cycle to 'chase' the other trajectory, which takes a considerable amount of time. An interesting observation is that the rate of geometric ergodicity increases significantly with the increased time separation scale μ. In other words, a larger time-scaling separation of the slow-fast dynamics make the law of (5.5) converge to its steady state distribution faster. To the best of our knowledge, this interesting phenomenon is not documented in the previous studies. We believe the reason is that a larger μ makes a trajectory move both slower near the slow manifold and closer to it, which significantly increase the chance for two trajectories to 'meet'. This is confirmed numerically by figure 7 bottom middle and right. The positions of 500 samples are plotted at which they are coupled for $\mu = 2$ and 12 respectively. We see that the larger μ makes the trajectories more likely to couple near the slow manifolds (the left and right branches of the limit cycle and its extensions).

5.4. SIR model with degenerate noise

In this subsection, we use an SIR model with degenerate noise to demonstrate how our algorithm can be adapted for SDEs with degenerate diffusion terms. For degenerate diffusions, only one step of the numerical algorithm does not produce a well-defined probability density function. We need more than one step to implement the maximal coupling.

Consider an epidemic model in which the whole population is divided into three distinct classes S (susceptible class), I (infected class), and R (recovered class), respectively. An SIR model with the population growth is given by

$$\begin{aligned} \mathrm{d}S &= (\alpha - \beta SI - \mu S)\,\mathrm{d}t \\ \mathrm{d}I &= (\beta SI - (\mu + \rho + \gamma)I)\,\mathrm{d}t \\ \mathrm{d}R &= (\gamma I - \mu R)\,\mathrm{d}t, \end{aligned} \tag{5.6}$$

where α is the population birth rate, μ is the disease-free death rate, ρ is the excess death rate for the infected class, γ is the recover rate for the infected population, and β is the effective contact rate between the susceptible class and infected class [14]. This model has been intensively studied. We refer [8, 33, 34] for a few representative references.

Assume that all the three classes are driven by the same random factor (such as temperature, humidity, etc). This gives the SDE a degenerate noise. Note that S and I in (5.6) are independent of R. So we consider the following SDE instead

$$\begin{aligned} \mathrm{d}S &= (\alpha - \beta SI - \mu S)\,\mathrm{d}t + \sigma S\,\mathrm{d}W_t \\ \mathrm{d}I &= (\beta SI - (\mu + \rho + \gamma)I)\,\mathrm{d}t + \sigma I\,\mathrm{d}W_t, \end{aligned} \tag{5.7}$$

where $\sigma > 0$ is the intensity of the white noise, and the two $\mathrm{d}W_t$ terms are from the same Brownian motion. See figure 8 left for the trajectory in $\mathbb{R}^2_+$.

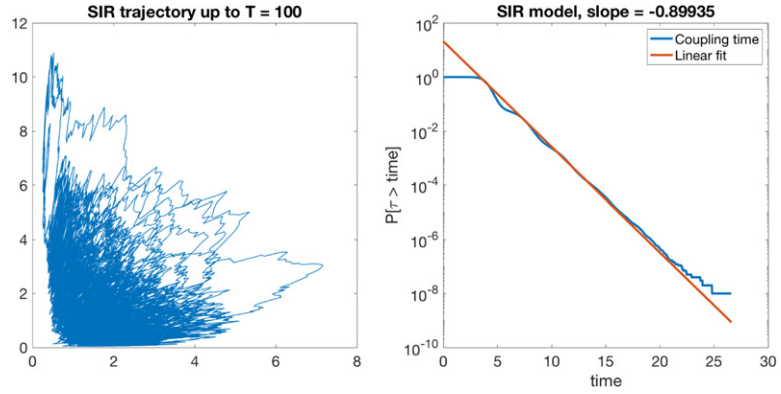

Figure 8. Left: trajectory of equation (5.7) up to $T = 100$. Right: coupling time distribution $\mathbb{P}[\tau_c > t]$ vs t in log-linear plot and linear function fitting. Parameters are $\alpha = 7$, $\beta = 3$, $\mu = 1$, $\rho = 1$, $\gamma = 2$, and $\sigma = 1$.

In [14], several results about the asymptotic behaviours of (5.7) are proved. Let

$$\lambda = \frac{\alpha\beta}{\mu} - \left(\mu + \rho + \gamma - \frac{\sigma^2}{2}\right).$$

If $\lambda > 0$, then (5.7) admits a non-degenerate invariant probability measure on $\mathbb{R}^2_+$. In addition, it was shown that (5.7) approaches to its invariant probability measure faster than any polynomial of t. This result is later improved in [46]. In this example, it is very challenging to construct an optimal Lyapunov function to control the two different factors simultaneously. The Lyapunov function of (5.7) must take high values when S and I are either too large or too small. A different approach is used in [46] to show the exponential ergodicity, but the resultant rate is still not quantitative.

We use algorithm 2 with an adaptation to the degenerate noise (which will be explained later) to examine the ergodicity of (5.7). The model parameters are set as $\alpha = 7$, $\beta = 3$, $\mu = 1$, $\rho = 1$, $\gamma = 2$, and $\sigma = 1$, the same as the example used in [14]. Note that the reflection coupling cannot be applied due to the degeneracy of the noise. In fact, for this set of parameters, the deterministic part of (5.7) converges to a unique equilibrium. With the same random noise being applied each time, any pair of stochastic trajectories of (5.7) will converge to each other, just as its deterministic part does. So in algorithm 2, we first use the synchronous coupling to make the two trajectories sufficiently close. Then we implement a 'two-step version' of the maximal coupling to check whether the two trajectories can couple after every two steps. The numerical algorithm we use is still the Euler–Maruyama method with the step size $h = 0.001$. The total sample size is $N = 10^8$. The coupling time distribution is demonstrated in figure 8 right. We can clearly see an exponential tail for $\mathbb{P}[\tau_c > t]$. The linear fitting of $\log\ \mathbb{P}[\tau_c > t]$ versus t gives a slope $\approx -0.533\,49$. Therefore, we conclude that (5.7) is indeed geometrically ergodic.

Now, we explain how to adapt algorithm 3 for the degenerate diffusions. Since the one-step transition probability density function of (5.7) is degenerate, the density functions $p^{(x)}$ and $p^{(y)}$ in algorithm 3 are not well-defined. Instead, we need to manually calculate the two-step transition probability density function and then run the maximal coupling for two successive steps. Hence, the output in algorithm 3 should be $(\mathcal{X}_{n+2}, \mathcal{Y}_{n+2})$ and $\tau_c = n_c h$. For convenience, we still use $p^{(x)}$ and $p^{(y)}$ to denote the respective probability density functions of $\mathcal{X}_{n+2}$ and $\mathcal{Y}_{n+2}$.

In this way, the two-step version of algorithm 3 is as follows: (i) sample $\mathcal{X}_{n+2}$ and calculate $W = Up^{(x)}(\mathcal{X}_{n+2})$; (ii) if $W \leqslant p^{(y)}(\mathcal{X}_{n+2})$, let $\mathcal{X}_{n+2} = \mathcal{Y}_{n+2}, \tau_c = (n+2)h$. Otherwise, sample $\mathcal{Y}_{n+2}$ and calculate $W' = Vp^{(y)}(\mathcal{Y}_{n+2})$ until $W' > p^{(x)}(\mathcal{Y}_{n+2})$. This method works for other similar problems with degenerate diffusions. If the noise is very degenerate, one may need to calculate the probability density function after more than two steps.

It is not easy to explicitly estimate the probability density function of the Euler–Maruyama method for two steps (or more). (One exception is the Langevin dynamics because the derivative of the position variable is a linear function of the velocity, which makes it possible to calculate an explicit probability density function; see the first author's another recent paper [15].) We need to use the transformation of probability density functions to calculate $p^{(x)}$ and $p^{(y)}$ at different points. Our implementation is as below.

Let $\bar{S}_n$ and $\bar{I}_n$ be the approximate values of S_n^h and I_n^h when running the Euler–Maruyama method. After one step iteration, we have

$$\begin{aligned}\bar{S}_{n+1} &= \bar{S}_n + (\alpha - \beta\bar{S}_n\bar{I}_n - \mu\bar{S}_n)h + \sigma\bar{S}_n\sqrt{h}N_1 := \widetilde{S}_{n+1} + \sigma\bar{S}_n\sqrt{h}N_1,\\ \bar{I}_{n+1} &= \bar{I}_n + (\beta\bar{S}_n\bar{I}_n - (\mu+\rho+\gamma)\bar{I}_n)h + \sigma\bar{I}_n\sqrt{h}N_1 := \widetilde{I}_{n+1} + \sigma\bar{I}_n\sqrt{h}N_1,\end{aligned}$$

where N_1 is a standard normal random variable. After two steps, with some calculations we have

$$\begin{aligned}\bar{S}_{n+2} &= \widetilde{S}_{n+1} + (\alpha - \beta\widetilde{S}_{n+1}\widetilde{I}_{n+1} - \mu\widetilde{S}_{n+1})h + R_S(N_1,N_2)\\ \bar{I}_{n+2} &= \widetilde{I}_{n+1} + (\beta\widetilde{S}_{n+1}\widetilde{I}_{n+1} - (\mu+\rho+\gamma)\widetilde{I}_{n+1})h + R_I(N_1,N_2),\end{aligned} \tag{5.8}$$

where N_1, N_2 are two independent standard normal random variables. The transformations R_S and R_I are as follows

$$\begin{aligned}R_S(N_1,N_2) = [&-\beta\sigma\bar{S}_nh^{3/2}\widetilde{I}_{n+1} - \beta\sigma\bar{I}_nh^{3/2}\widetilde{S}_{n+1} - \mu\sigma\bar{S}_nh^{3/2} + \sigma\bar{S}_nh^{1/2}]N_1\\ &+ \sigma\widetilde{S}_{n+1}h^{1/2}N_2 - \beta\sigma^2\bar{S}_n\bar{I}_nh^2N_1^2 + \sigma^2\bar{S}_nhN_1N_2\end{aligned} \tag{5.9}$$

and

$$\begin{aligned}R_I(N_1,N_2) = [&\beta\sigma\bar{S}_nh^{3/2}\widetilde{I}_{n+1} + \beta\sigma\bar{I}_nh^{3/2}\widetilde{S}_{n+1} - (\mu+\rho+\gamma)\sigma\bar{I}_nh^{3/2}\\ &+ \sigma\bar{I}_nh^{1/2}]N_1 + \sigma\widetilde{I}_{n+1}h^{1/2}N_2 - \beta\sigma^2\bar{S}_n\bar{I}_nh^2N_1^2 + \sigma^2\bar{I}_nhN_1N_2.\end{aligned} \tag{5.10}$$

For h sufficiently small, the transformation $(N_1,N_2) \mapsto (R_S,R_I)$ is close to a linear transformation since all the coefficients of quadratic terms are significantly smaller than that of the linear terms. Hence, we treat this transformation as invertible when calculating the probability density function.

By the elementary probability, it is easy to see that the joint probability density function $p(R_S,R_I)$ is given by

$$p(R_S,R_I) = |J|^{-1}p^{\text{norm}}(\bar{N}_1,\bar{N}_2), \tag{5.11}$$

where J is the Jacobian matrix of the transformation $(N_1,N_2) \mapsto (R_S,R_I)$, p^{norm} is the probability density function of the 2D standard normal random variable, and $\bar{N}_1,\bar{N}_2$ are the values of random variables N_1 and N_2 that produce (R_S,R_I).

Now, let $\mathcal{X}_n^h = (\bar{S}_n^x,\bar{I}_n^x)$ and $\mathcal{Y}_n^h = (\bar{S}_n^y,\bar{I}_n^y)$ be the two numerical trajectories that need to be coupled. Let p^x and p^y be the probability density functions of $\mathcal{X}_{n+2}^h$ and $\mathcal{Y}_{n+2}^h$, respectively. In algorithm 3, we need to compute four probability densities: $p^{(x)}(\mathcal{X}_{n+2}^h)$, $p^{(x)}(\mathcal{Y}_{n+2}^h)$, $p^{(y)}(\mathcal{X}_{n+2}^h)$,

and $p^{(y)}(\mathcal{Y}^h_{n+2})$. Since the normal random variables N_1 and N_2 are already known when sampling $\mathcal{X}^h_{n+2}$, $p^{(x)}(\mathcal{X}^h_{n+2})$ is given by (5.11) directly. For $p^{(x)}(\mathcal{Y}^h_{n+2})$, we need to calculate the 'effective' (R^y_S, R^y_I) from (5.8) for $\mathcal{X}^h_{n+2}$, which are the 'effective random terms' for $\mathcal{X}^h_{n+2}$ to produce $\mathcal{Y}^h_{n+2}$. This is done by solving the following equations

$$\begin{aligned}\bar{S}^y_{n+2} &= \widetilde{S}^x_{n+1} + (\alpha - \beta\widetilde{S}^x_{n+1}\widetilde{I}^x_{n+1} - \mu\widetilde{S}^x_{n+1})h + R^y_S(N^y_1, N^y_2)\\ \bar{I}^y_{n+2} &= \widetilde{I}^x_{n+1} + (\beta\widetilde{S}^x_{n+1}\widetilde{I}^x_{n+1} - (\mu+\rho+\gamma)\widetilde{I}^x_{n+1})h + R^y_I(N^y_1, N^y_2).\end{aligned}$$

Then we solve (N^y_1, N^y_2) by numerically solving equation (5.9) and (5.10) for (R^y_S, R^y_I). We use Newton's method which converges after less than 5 steps. This gives the 'effective normal random variables' for $\mathcal{X}^h_{n+2}$ to produce $\mathcal{Y}^h_{n+2}$. The probability density function $p^{(x)}(\mathcal{Y}^h_{n+2})$ is obtained by applying the transformation (5.11) to the numerically solved (N^y_1, N^y_2). Computations of $p^{(y)}(\mathcal{X}^h_{n+2})$ and $p^{(y)}(\mathcal{Y}^h_{n+2})$ are analogous.

We remark that this is a representative example because many random dynamical systems in various different settings admit random attractors [2, 13, 50, 53, 54]. This means that any trajectory along the same Brownian sample path, denoted by ω, will converge to an ω-dependent set $A(\omega)$. If $A(\omega)$ is a stable equilibrium, the synchronous coupling can bring any two trajectories close to each other. It is also called reliability by some authors [41]. When the two trajectories close enough, one can shift to the maximal coupling to make them collapse together. This approach builds some additional connections between the theories of random dynamical systems and SDEs.

5.5. Coupled stochastic FitzHugh–Nagumo model

A significant advantage of the coupling method used in this paper is that it is relatively dimension-free. In contrast, approaches relying on the discretization of the generator is extremely difficult when dealing with higher dimensional problems. In this subsection, we consider a very high dimensional example: the stochastic FitzHugh–Nagumo (FHN) model, for which the many stochastically FHN oscillators are coupled. It is well known that the FHN model is a nonlinear model that models the periodic evolution of the membrane potential of a spiking neuron under external stimulations. For a single neuron, this model is a 2D dynamical system with additive noise

$$\begin{aligned}\mu\,\mathrm{d}u &= \left(u - \frac{1}{3}u^3 - v\right)\,\mathrm{d}t + \sqrt{\mu}\sigma\,\mathrm{d}W^{(1)}_t\\ \mathrm{d}v &= (u+a)\,\mathrm{d}t + \sigma\,\mathrm{d}W^{(2)}_t,\end{aligned} \tag{5.12}$$

where u represents the membrane potential, v is a recovery variable, and $W^{(1)}_t, W^{(2)}_t$ are two independent Brownian motions. When $a = 1.05$, the deterministic system admits a stable equilibrium with a small basin of attraction. Intermittent limit cycles can be triggered by suitable random perturbations which are strong enough to drive the system out from the basin of attraction.

Consider 50 coupled equation (5.12) with both the nearest-neighbour interaction and a mean-field interaction. Similar as in [11], let $v = \sqrt{\mu}v$ be the new recovery variable. This

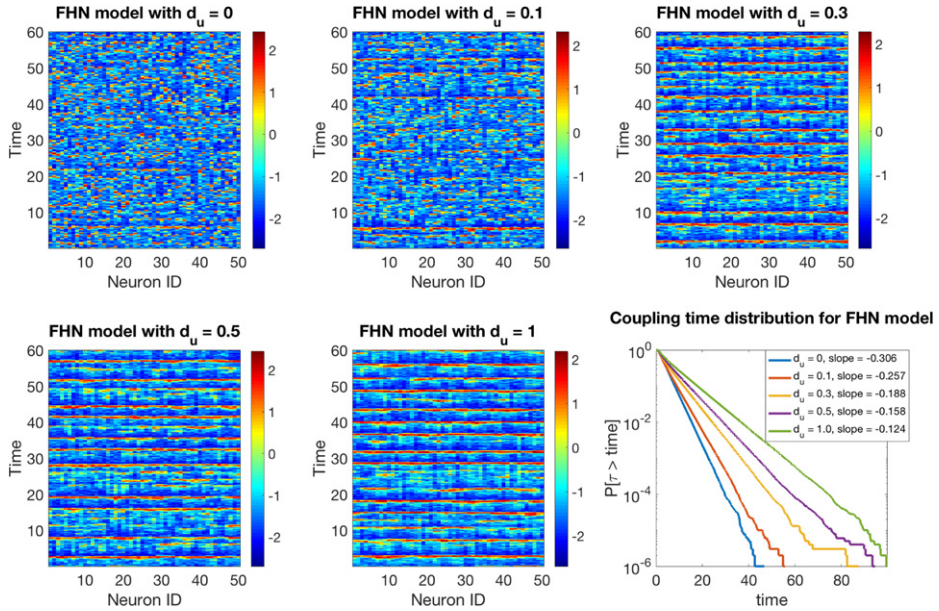

Figure 9. Panel I–V: time evolutions of membrane potential of 50 coupled neurons in FHN model. Coupling strength d_u takes value $0, 0.1, 0.3, 0.5$, and 1 in five figures. Different colours means different membrane potentials (see the colour bar beside). X-axis: neuron ID. Y-axis: time. Panel VI: coupling time distributions of FHN model with five different d_u values in a log-linear plot.

gives the coupled FHN oscillator

$$\begin{aligned} \mathrm{d}u_i &= \left(\frac{1}{\mu}u_i - \frac{1}{3\mu}u_i^3 - \frac{1}{\sqrt{\mu}}v_i + \frac{d_u}{\mu}(u_{i+1} + u_{i-1} - 2u_i) + \frac{w}{\mu}(\bar{u} - u_i)\right)\mathrm{d}t \\ &\quad + \frac{\sigma}{\sqrt{\mu}}\mathrm{d}W_t^{(2i-1)} \\ \mathrm{d}v_i &= \left(\frac{1}{\sqrt{\mu}}u_i + \frac{a}{\sqrt{\mu}}\right)\mathrm{d}t + \frac{\sigma}{\sqrt{\mu}}\mathrm{d}W_t^{(2i)} \end{aligned} \tag{5.13}$$

for $i = 1, \ldots, 50$, where d_u is the nearest-neighbour coupling strength, w is the mean field coupling strength, $W_t^{(1)}, \ldots, W_t^{(100)}$ are independent Brownian motions, and

$$\bar{u} = \frac{1}{50}\sum_{i=1}^{50} u_i$$

is the mean membrane potential. We set $u_0 = u_{50}$ and $u_{51} = u_1$ so that the 50 neurons are connected as a ring. We would like to use this example to demonstrate the strength of our algorithm when dealing with the high-dimensional problems. The connection between the ergodicity and degree of synchrony will also be discussed.

In our simulations, we choose parameters $w = 0.4$, $\mu = 0.05$, and $\sigma = 0.6$. These parameters are similar to those in [11]. The main control parameter is d_u. A higher d_u means a stronger nearest-neighbour coupling, which gives a more synchronized dynamics. See figure 9 panel

I–V for the time evolutions of the membrane potential with different d_u. We see that a higher d_u makes the membrane potentials of the 50 neurons evolve more coherently.

We use the Euler–Maruyama scheme in our simulations with the step size $h = 0.001$. We run algorithm 2 with $N = 10^6$ samples for $d_u = 0, 0.1, 0.3, 0.5$, and 1 to compute the slopes of exponential tails of the distribution of coupling times. See figure 9 panel VI for a comparison of the coupling time distributions and slopes. We see that higher d_u's provide longer coupling times, and hence lower rates of geometric ergodicity. Heuristically, this phenomenon is caused by the phase lock. In the presence of strong synchronization, the trajectories are attracted to the neighbourhood of a high dimensional limit cycle and follow it as time evolves. When running the coupling process, the two independent trajectories can be attracted to difference phases of this limit cycle. When this happens, it will take longer times for the two trajectories to couple, as one trajectory needs to diffuse by itself to 'chase' the other one along the limit cycle.

6. Conclusion and further discussions

The geometric ergodicity is an important property of a stochastic process with an infinitesimal generator. It measures the mixing effect given by a combination of the underlying deterministic dynamics and the random perturbations. In this paper, based on the coupling technique, we propose a probabilistic method to numerically compute the rate of geometric ergodicity. Some straightforward arguments show that the lower bound of the rate can be estimated by computing the exponential tail of the coupling times. In addition, we find that the upper bound of the geometric convergence rate can also be estimated by computing the first exit time with respect to a sequence of disjoint sets pairs. Compared with the traditional method that looks for the eigenvalues of the discretized infinitesimal generator, our method is relatively dimension-free. It works well when the dimension of the phase space becomes too high for the grid-based method to handle.

As numerical examples, we study several deterministic dynamical systems with additive noise perturbations. One interesting finding is that the coupling time distributions under noise magnitudes can provide a lot of information about the deterministic dynamics. As demonstrated in section 4, the random perturbed systems admit different convergence rate versus noise curves when their underlying deterministic dynamics admit different degrees of chaos. In other words, the coupling times provide some data-driven inference of the underlying deterministic dynamics. Since the coupling method is relatively dimension-free, we expect that this approach can be used to characterize some high-dimensional deterministic dynamical systems, such as the gradient flows of high-dimensional potential functions. We plan to further explore along this direction in future works.

Despite the success of the many examples, the coupling method has its own limitations. Although there are some known results about coupling with degenerate noise, such as the coupling for the Langevin dynamics [19] or the Hamiltonian Monte Carlo method [7]. When the noise is highly degenerate, it becomes difficult to design an effective coupling scheme. In addition, with degenerate noise, the numerical maximal coupling updates become significantly difficult, as one needs to compute the probability density function of several consecutive updates in order to get a non-degenerate probability density function. As shown in section 5.4, even the implementation of a relatively simple 2D example has some nontrivial overhead. At each step, one needs to run a nonlinear equation solver twice to check the probability of coupling. In this situation, a 'weaker' approach based on the numerical return time and analytical minorization condition works better; see the first author's earlier paper [39]. The method in [39] can numerically check the qualitative rate of ergodicity (geometric or sub-geometric),

although in general it does not give a useful bound for the rate of geometric ergodicity. The first author is currently writing a separate paper to extend the method in [39] to the case of SDEs with highly degenerate noise terms.

Acknowledgments

The authors would like to thank the referees for their valuable and constructive comments which significantly improve the quality of this paper in both presentation and substance. YL was partially supported by NSF DMS-1813246. SW was partially supported by NSFC Grants 11771026 and 11471344, and acknowledges PIMS-CANSSI postdoctoral fellowship.

References

[1] Aldous D 1983 Random walks on finite groups and rapidly mixing Markov chains *Séminaire de Probabilités XVII 1981/82* (Berlin: Springer) pp 243–97
[2] Arnold L 1995 Random dynamical systems *Dynamical Systems* (Berlin: Springer) pp 1–43
[3] Ausloos M and Dirickx M 2006 *The Logistic Map and the Route to Chaos: From the Beginnings to Modern Applications* (Berlin: Springer)
[4] Bakry D and Émery M 1985 Diffusions hypercontractives *Séminaire de Probabilités XIX 1983/84* (Berlin: Springer) pp 177–206
[5] Blumenthal A, Xue J and Young L-S 2017 Lyapunov exponents for random perturbations of some area-preserving maps including the standard map *Ann. Math.* **185** 285–310
[6] Blumenthal A, Xue J and Young L-S 2018 Lyapunov exponents and correlation decay for random perturbations of some prototypical 2D maps *Commun. Math. Phys.* **359** 347–73
[7] Bou-Rabee N, Eberle A and Zimmer R 2018 Coupling and convergence for Hamiltonian Monte Carlo (arXiv:1805.00452)
[8] Capasso V 1993 *Mathematical Structures of Epidemic Systems* vol 88 (Berlin: Springer)
[9] Chen M-F and Wang F-Y 1997 Estimation of spectral gap for elliptic operators *Transactions of the American Mathematical Society* **349** 1239–67
[10] Chen M 1996 Estimation of spectral gap for Markov chains *Acta Math. Sin.* **12** 337–60
[11] Chen N, Majda A J and Tong X T 2019 Spatial localization for nonlinear dynamical stochastic models for excitable media (arXiv:1901.07318)
[12] Cranston M 1991 Gradient estimates on manifolds using coupling *J. Funct. Anal.* **99** 110–24
[13] Debussche A 1997 On the finite dimensionality of random attractors *Stoch. Anal. Appl.* **15** 473–91
[14] Thanh Dieu N, Nguyen D H, Huu Du N and Yin G G 2016 Classification of asymptotic behavior in a stochastic SIR model *SIAM J. Appl. Math.* **15** 1062–84
[15] Dobson M, Zhai J and Li Y 2019 Using coupling methods to estimate sample quality for stochastic differential equations (arXiv:1912.10339)
[16] Doeblin W 1938 Exposé de la théorie des chaınes simples constantes de Markov á un nombre fini d'états *Mathématique de l'Union Interbalkanique* **2** 78–80
[17] Eberle A 2011 Reflection coupling and Wasserstein contractivity without convexity *C. R. Math.* **349** 1101–4
[18] Eberle A 2016 Reflection couplings and contraction rates for diffusions *Prob. Theory Relat. Fields* **166** 851–86
[19] Eberle A, Guillin A, Zimmer R *et al* 2019 Couplings and quantitative contraction rates for Langevin dynamics *Anal. Prob.* **47** 1982–2010
[20] Iosifovich Freidlin M and Wentzell A D 1998 Random perturbations *Random Perturbations of Dynamical Systems* (Berlin: Springer) pp 15–43
[21] Griffeath D 1975 A maximal coupling for Markov chains *Prob. Theory Relat. Fields* **31** 95–106
[22] Hairer M 2016 Convergence of Markov processes *Lecture Notes* University of Warwick www.hairer.org/notes/Convergence.pdf

[23] Hairer M and Mattingly J C 2011 Yet another look at Harris' ergodic theorem for Markov chains *Seminar on Stochastic Analysis, Random Fields and Applications VI* (Berlin: Springer) pp 109–17
[24] Holley R and Stroock D W 1987 Logarithmic Sobolev inequalities and stochastic Ising models *J. Stat. Phys.* **46** 1159–94
[25] Hsu E P 2002 *Stochastic Analysis on Manifolds* vol 38 (Providence, RI: American Mathematical Society)
[26] Hsu E P and Sturm K-T 2013 Maximal coupling of Euclidean Brownian motions *Communications in Mathematics and Statistics* **1** 93–104
[27] Iacobucci A, Olla S and Stoltz G 2019 Convergence rates for nonequilibrium Langevin dynamics *Annales mathématiques du Québec* **43** 73–98
[28] Jacob P E, O'Leary J and Atchadé Y F 2017 Unbiased Markov chain Monte Carlo with couplings (arXiv:1708.03625)
[29] Johndrow J E and Mattingly J C 2017 Error bounds for approximations of Markov chains used in Bayesian sampling (arXiv:1711.05382)
[30] Johnson V E 1998 A coupling-regeneration scheme for diagnosing convergence in Markov chain Monte Carlo algorithms *J. Am. Stat. Assoc.* **93** 238–48
[31] Katok A and Hasselblatt B 1995 Introduction to the modern theory of dynamical systems *Encyclopedia of Mathematics and its Applications* vol 54 (Cambridge: Cambridge University Press)
[32] Kendall W S 1989 Coupled Brownian motions and partial domain monotonicity for the Neumann heat kernel *J. Funct. Anal.* **86** 226–36
[33] Kermack W O and Anderson M K G 1991 Contributions to the mathematical theory of epidemics–I. 1927 *Bull. Math. Biol.* **53** 33
[34] Ogilvy Kermack W and McKendrick A G 1932 Contributions to the mathematical theory of epidemics. II.–The problem of endemicity *Proc. R. Soc.* A **138** 55–83
[35] Kloeden P E and Platen E 2013 *Numerical Solution of Stochastic Differential Equations* vol 23 (Berlin: Springer)
[36] Latorre J C, Pavliotis G A and Kramer P R 2013 Corrections to Einstein's relation for Brownian motion in a tilted periodic potential *J. Stat. Phys.* **150** 776–803
[37] Lelievre T and Stoltz G 2016 Partial differential equations and stochastic methods in molecular dynamics *Acta Numerica* **25** 681–880
[38] Li Y 2015 On the stochastic behaviors of locally confined particle systems *Chaos* **25** 073121
[39] Li Y and Xu H 2017 Numerical simulation of polynomial-speed convergence phenomenon *J. Stat. Phys.* **169** 697–729
[40] Lin K K 2004 Convergence of invariant densities in the small-noise limit *Nonlinearity* **18** 659–83
[41] Lin K K, Shea-Brown E and Young L-S 2009 Reliability of coupled oscillators *J. Nonlinear Sci.* **19** 497–545
[42] Lindvall T 2002 *Lectures on the Coupling Method* (Courier Corporation) (New York: Dover)
[43] Lindvall T, Rogers L C G *et al* 1986 Coupling of multidimensional diffusions by reflection *Annals of Probability* **14** 860–72
[44] Meyn S P and Richard L T 2012 *Markov Chains and Stochastic Stability* (Berlin: Springer)
[45] Mitrophanov A Y 2005 Sensitivity and convergence of uniformly ergodic Markov chains *J. Appl. Probab.* **42** 1003–14
[46] Nguyen D H, Nguyen N N and Yin G 2020 General nonlinear stochastic systems motivated by chemostat models: complete characterization of long-time behavior, optimal controls, and applications to wastewater treatment *Stoch. Process. Appl.* **130** 4608–42
[47] Pitman J W 1976 On coupling of Markov chains *Probability Theory and Related Fields* **35** 315–22
[48] Risken H 1989 The Fokker–Planck equation *Methods of Solution and Applications* vol 18 (Berlin: Springer)
[49] Roussel J and Stoltz G 2018 Spectral methods for Langevin dynamics and associated error estimates *ESAIM: Math. Modelling Numer. Anal.* **52** 1051–83
[50] Schmallfuß B 1997 The random attractor of the stochastic Lorenz system *Zeitschrift für angewandte Mathematik und Physik ZAMP* **48** 951–75
[51] Viana M 1997 Stochastic dynamics of deterministic systems *Braz. Math. Colloq.* (Rio de Janeiro: IMPA) vol 21
[52] Walters P 1982 *An Introduction to Ergodic Theory* (Berlin: Springer)

[53] Wang R 2020 Long-time dynamics of stochastic lattice plate equations with nonlinear noise and damping *J. Dyn. Differ. Equ.* 1–37
[54] Wang R, Shi L and Wang B 2019 Asymptotic behavior of fractional nonclassical diffusion equations driven by nonlinear colored noise on *Nonlinearity* **32** 4524
[55] Young L-S 1999 Recurrence times and rates of mixing *Isr. J. Math.* **110** 153–88